

Research Paper

# Modeling of flow characteristics in 3D rough rock fracture with geometry changes under confining stresses

Yuedu Chen<sup>a,b,c</sup>, A.P.S. Selvadurai<sup>c</sup>, Zhihong Zhao<sup>a</sup><sup>a</sup> Department of Civil Engineering, Tsinghua University, Beijing 100084, China<sup>b</sup> College of Mining Engineering, Taiyuan University of Technology, Taiyuan, Shanxi 030024, China<sup>c</sup> Department of Civil Engineering and Applied Mechanics, McGill University, 817 Sherbrooke Street, West Montréal, QC H3A 0C3, Canada

## ARTICLE INFO

## Keywords:

Flow simulations  
 Rough fracture  
 Confining stress  
 Fracture geometries  
 Non-Darcy flow  
 N-S equations

## ABSTRACT

A series of fracture geometries of an artificially tensile fractured sandstone, measured during the hydraulic tests at increasing confining stresses, were adopted to build 3D fracture models. At each stress level, four groups of flow simulations with increasing injection flow rates were conducted, to examine how voids and contact alterations due to stress changes affect the flow characteristics within the fracture. The results show that the simulated normalized apparent transmissivity matched well with that measured from hydraulic tests, and both them decrease nonlinearly with increasing confining stress. The alterations in fracture geometries due to stress changes increase the heterogeneities of flow characteristics in 3D fractures, including flow rates, streamlines, water pressure. The streamlines become more channeled with observable tortuosity under high stress. The stress induced increase in contact and the occurrence of eddy flow enhance the non-linearity of pressure drop. The decrease of both apertures and sharp geometries under high stress reduces the range of eddy flows, which delays the occurrence of significant inertial effects and results in the increase of critical Reynolds numbers. These features are demonstrated well using an idealized 3D representative geometric including both the asperity contacts and voids.

## 1. Introduction

Fluid flow and related transport characteristics through fractured rock masses have to be considered in many underground rock engineering endeavors, including tunnel excavation, hydraulic engineering, geothermal exploitation, hazardous waste isolation, etc. (Zhao and Brown 1992; Jing 2003; Rutqvist and Stephansson 2003; Zhao et al. 2011; Zhang and Nemeik 2013; Zhao 2014; Develi and Babadagli 2015; Selvadurai et al. 2015, 2018; Singh et al. 2015; Xiong et al. 2018) (Fig. 1-a). The knowledge of the flow behavior through the single rough fracture forms the basis for the representation of the flow behavior in a complicated fractured rock mass, especially after redistribution of the in-situ stresses (Fig. 1-b).

Fractures are intrinsically heterogeneous, and the complicated geometries (void spaces and asperity contacts) existing non-uniformly between two contacting fracture surfaces are easily altered thermally, geochemically and deformed under applied stress, which complicates the flow process and significantly affect fluid flow through rock fractures (Pyrak-Nolte and Nolte 2016) (Fig. 1-c). Although considerable efforts in theoretical, empirical and experimental works have provided the

macroscopic knowledge of the changes in flow behavior due to variations in the fracture geometries (Tsang and Witherspoon 1981; Schrauf and Evans 1986; Zimmerman et al. 1992; Detwiler et al. 2000; Li et al. 2008, 2016; Ishibashi et al. 2015; Chen et al. 2017; Stoll et al. 2019), the absence of monitored results of the internal phenomena cannot provide an adequate understanding of their influences. More information is required on how the streamlines or water pressure distribution throughout the fracture changes flow velocities around the contact spots and aperture space, etc., and how these affect the flow characteristics, especially under progressively increasing confining stresses.

Numerical approaches, due to their convenience and flexibility in simulating complicated geometries and flow conditions, have been widely used as a practical method to solve flow simulations in rough fractures. There are numerous approaches regarding flow simulations through the rough fracture, and roughly classed in Table.1, based on fracture dimensions (2D and 3D), fracture types (hypothetical and real fractures), or the flow models (N-S equations, Reynolds equations, etc). The commonly used 2D fracture model, formed by two asperities profiles, are proposed to investigate the effect of surface roughness on the flow behaviors through rock fractures by ignoring the transverse flow in

E-mail address: [reading0901@tsinghua.edu.cn](mailto:reading0901@tsinghua.edu.cn) (Y. Chen).

<https://doi.org/10.1016/j.compgeo.2020.103910>

Received 7 August 2020; Received in revised form 7 October 2020; Accepted 27 October 2020

Available online 24 November 2020

0266-352X/© 2020 Elsevier Ltd. All rights reserved.

x- or y- axis direction (Nazridoust et al. 2006; Cardenas et al. 2007; Koyama et al. 2008; Xie et al. 2015; Zou et al. 2015). These profiles are chosen directly from real rock fractures or artificially defined using mathematical algorithms, such as fractal algorithms, wavelet analysis, and so on. Although such 2D models provide an important conceptual understanding of surface fluctuation or waves effects on flow complexities, the absence of the changes in geometry, including the contact regions and the variable aperture space in the vertical and horizontal directions, caused by a mechanical, geochemical and thermal process, cannot be fully incorporated, and these deficiencies can lead to the lack of channeling phenomena or the incorrect interpretation of the flow characteristics of a fracture. Another widely used 2D model, simplified from the 3D rock fractures by ignoring the flow in z- axis direction, is recorded in numerous works. It assumes that the joint is made up of a series of grid cells, and the aperture in each grid point of the cell is denoted by a local aperture (Koyama et al. 2009; Indraratna et al. 2015; Pyrak-Nolte and Nolte 2016; Mofakham et al. 2018; Niya and Selvadurai 2019). Although the heterogeneous aperture and contact distributions can be considered, the significant impacts of mid-surface roughness or vertical tortuosity are absent (Zou et al. 2017a). Many current studies focused on the flow simulations in 3D rock fractures to compensate for the above shortcomings (Javadi et al. 2010; Xiong et al. 2011; Wang et al. 2016; Huang et al. 2017; Zou et al. 2017a; Kong and Chen 2018; Liu et al. 2020). However, these 3D models are mainly the hypothetical fractures, which are artificially made of self-similar fractures, or composed of a series of grid blocks with varying height, or built through simply extruding the scanned surface upwards in the z- direction (Chen and Zhao 2020), all of them are quite different from the spatial

geometries in 3D real fractures, resulting in unreasonable local flow velocities or inner water pressure distributions in the rough fracture. Thus, conducting the flow simulations in 3D real rock fractures is necessary.

The Reynolds equation was widely used in simulating the fluid flow inside fractures. However, it was derived based on an approximation of the incompressible Navier-Stokes (NS) equation and are applicable only under different simplifying assumptions on the fracture geometries and the fluid flow regime (Mofakham et al. 2018; Niya and Selvadurai 2019), such as the low Reynolds number ( $Re$ ) flow that the inertial forces in the fluid are negligibly small compared with the viscous and pressure forces (Koyama et al. 2008; Selvadurai et al. 2017), or the void spaces between the two fracture surfaces are made up of several local parallel-plate elements (Xiong et al. 2011). These assumptions may overestimate or underestimate the flow rate and result in deviations from the actual flow from reality for the flow through a rough fracture. To adequately consider the combined effects of the complicated fracture geometries and inertial terms, the full Navier-Stokes equation (N-S) is adopted in flow simulations in the 3D fractures (Zimmerman et al. 2004; Crandall et al. 2010; Javadi et al. 2010; Xiong et al. 2011; Wang et al. 2015; Zou et al. 2017a; Kong and Chen 2018). These studies illustrated the influence of roughness, fracture geometries, and inertial effects on flow behaviors in 3D rock fractures. However, the impacts of the mechanical loading on the changes of void spaces and contact, as well as their effects on the flow characteristics in the 3D real rock fractures have not been solved using the N-S equations to the authors' knowledge.

Motivated by this, a series of fracture geometries of an artificially tensile fractured and re-assembled sandstone sample, measured during

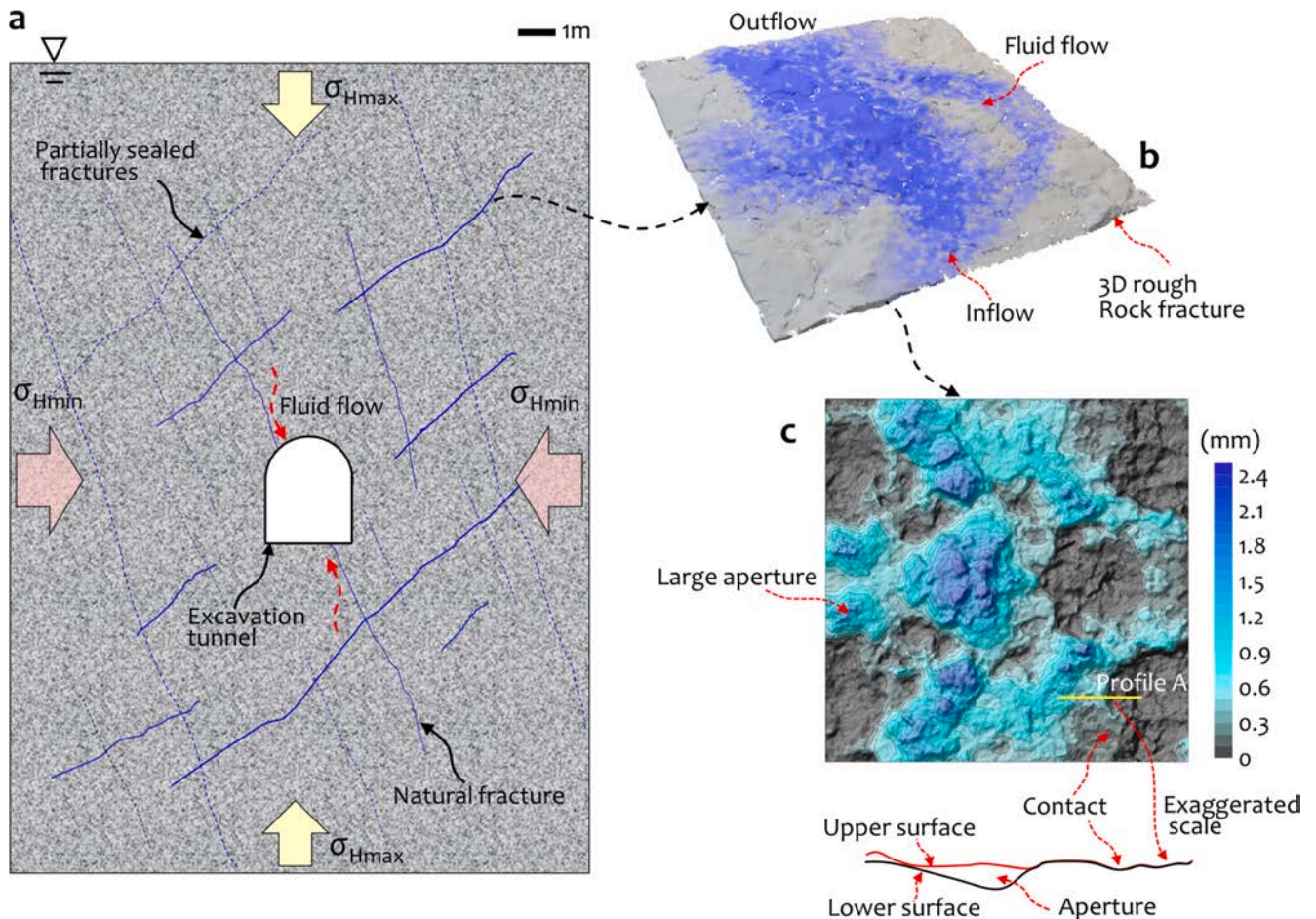


Fig. 1. (a) Schematic diagram of the underground water inflow into the tunnel excavation through the surrounding fractured rock mass, (b) Illustration of the fluid flow through the 3D rough rock fracture, (c) Fracture geometries distribution characteristics of the 3D rough rock fracture.

**Table 1**  
Methods regarding to the flow simulations of rough single fracture.

References	Fracture type	Dimension	Governing equations	Fracture geometries considered	Confine stress considered	Test validate
Xie et al. (2015), Nazridoust et al. (2006)	Hypothetical fracture	2D	N-S equations	Roughness and aperture	No	No
Wang et al.(2016)	Self-affine fracture	3D	Lattice Boltzmann method	Roughness	No	No
Huang et al. (2017)	Self-affine fracture	3D	Reynolds equation	Roughness	No	No
Kong and Chen (2018)	Self-affine fracture	3D	N-S equations	Roughness and aperture	No	No
Mofakham et al. (2018)	Discrete cell	2D	Cubic Law	Roughness, aperture and contact	No	Yes
Niya and Selvadurai (2019)	Discrete cell	2D	Stokes' equation	Roughness, aperture and contact	No	No
Indraratna et al. (2015)	Discrete cell	2D	N-S equations	Roughness, aperture and contact	Yes	No
Koyama et al. (2008)	Fracture profile	2D	N-S equations Reynolds equation	Roughness	No	No
Zou et al. (2015)	Fracture profile	2D	N-S equations	Roughness	No	No
Zou et al. (2017a; 2017b)	Hypothetical fracture	3D	N-S equations	Roughness, aperture and contact	No	No
Pyrak-Nolte and Nolte (2016)	Discrete cell	2D	linear flow equations	Roughness, aperture and contact	Yes	Yes
Javadi et al. (2010)	Hypothetical fracture (grid block)	3D	N-S equations	Roughness and aperture	No	No
Xiong et al. (2011)	Hypothetical fracture (grid block)	3D	N-S equations	Roughness, aperture and contact	Yes	Yes

the hydraulic tests at increasing confine stresses, were adopted to build 3D real fracture models; and flow simulations through such fracture models under increasing flow rates were solved using the Navier-Stokes equations, to investigate the impacts of the confine stress loading induced variable voids spaces and contact on the flow behaviors, including the streamlines, flow velocities, inner water pressure distributions, as well as the non-Darcy flow behaviors. The simulated apparent transmissivity in 3D real rock fractures under increasing confine stress are compared with that measured from hydraulic flow tests. A simplified 3D representative micro-model was built to demonstrate the mechanism by fracture geometries influences the water pressure distribution and non-Darcy in the 3D real fracture models. The results can advance our understanding of the influence of mechanical loading on the flow behaviors in 3D real fractured rocks, which is significant to lots of underground rock engineering.

## 2. Theoretical relevant to flow through rough fracture

### 2.1. Governing equations

The computational modelling of flow in a 3D real rough fracture was achieved by solving the Navier-Stokes equations (NSE) (Xiong et al. 2018), which are governed by the equations of mass and momentum conservation. For stable, incompressible and isothermal single Newtonian fluid flow, the NSE can be written as (Bear 1972; Zimmerman and Bodvarsson 1996):

$$\rho(\mathbf{u} \cdot \nabla)\mathbf{u} + \nabla P = \mu \nabla^2 \mathbf{u} \tag{1}$$

$$\nabla \cdot \mathbf{u} = 0 \tag{2}$$

where  $\mathbf{u}$ ,  $P$ ,  $\rho$  and  $\mu$  represent the flow velocity vector, the fluid pressure, the fluid density, and the dynamic viscosity, respectively. In Eq. (1), the term  $\mu \nabla^2 \mathbf{u}$  represents the viscous force, and the convective acceleration terms  $(\mathbf{u} \cdot \nabla)\mathbf{u}$ , representing the inertial forces acting on the fluid, giving

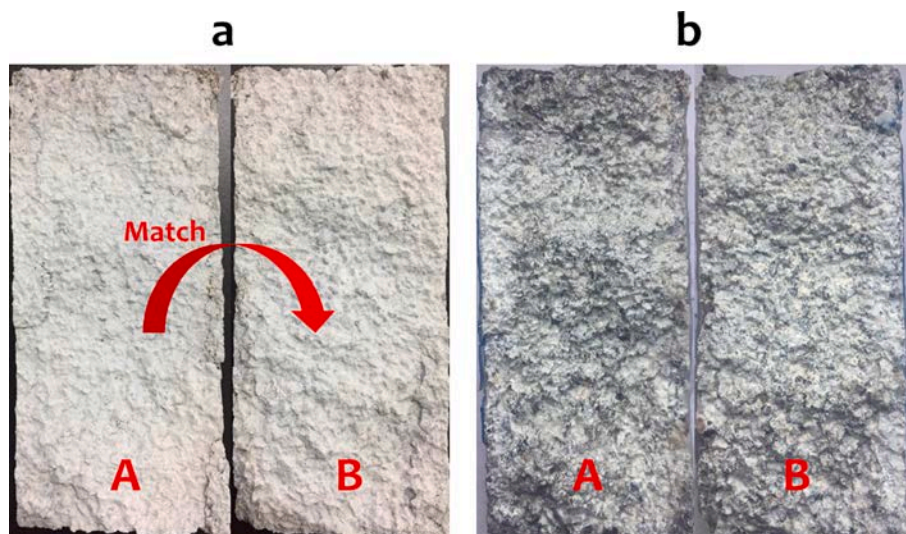


Fig. 2. Two rough surfaces of the test sandstone sample before (a) and after (b) the test.

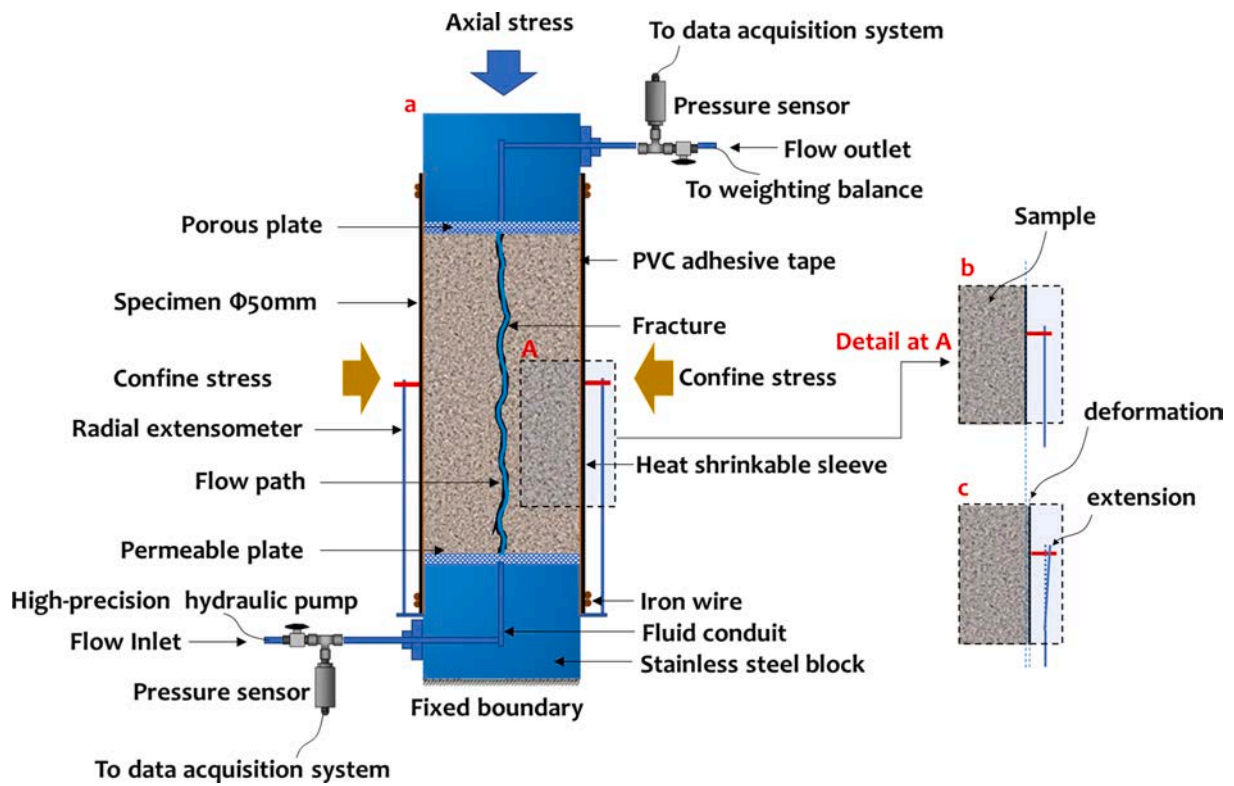


Fig. 3. Schematic diagram of the hydraulic flow tests by using the servo-controlled tri-axial system.

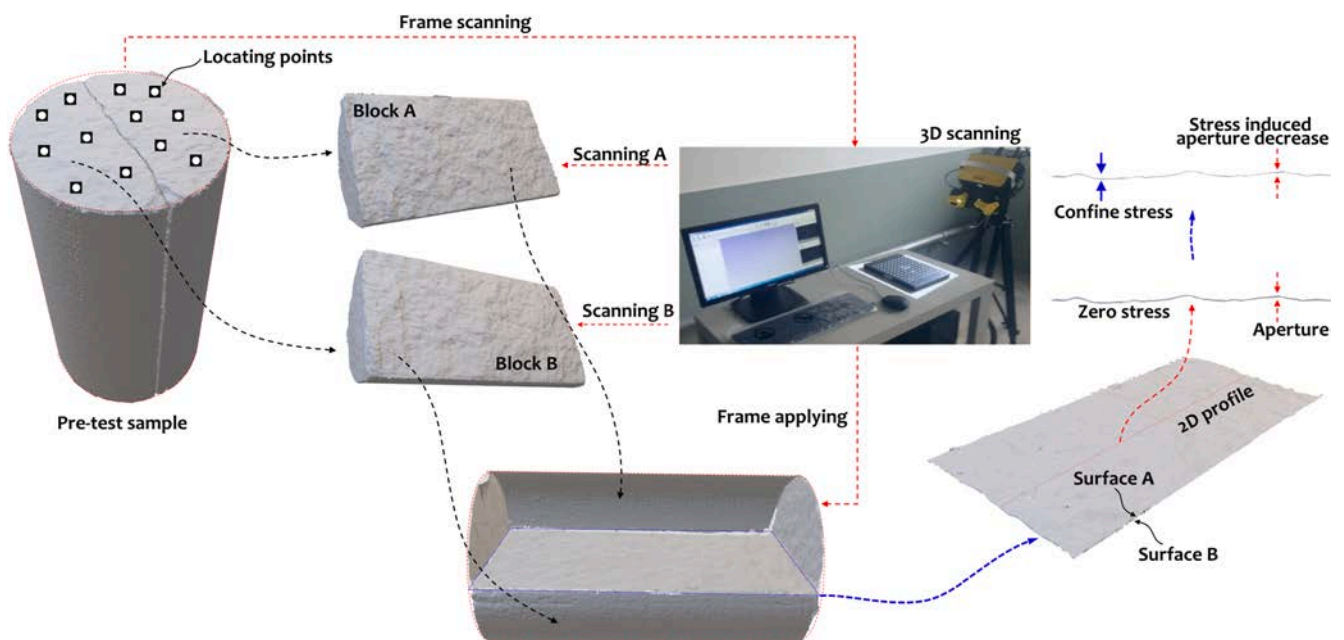


Fig. 4. Measurement procedures of the fracture aperture of the single rough rock fracture.

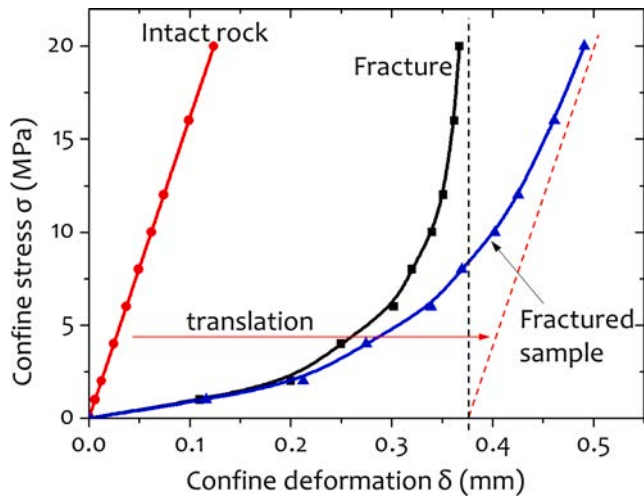


Fig. 5. Experimentally measured deformation of the fractured granite under increasing confine stress. (Dashed black lines mean the growth bound of the value).

rise to the nonlinearity of the equation and increase the computational cost.

2.2. Flow characterization

In certain cases, where the inertial forces in the fluid are negligibly small compared with the viscous and pressure forces, the Eq. (1) can be reduced to the Stokes' equation  $\mu \nabla^2 u - \nabla P = 0$ , which is suitable for simulating low Reynolds number ( $Re$ ) flow through the regular geometries. Based on Stokes's equations, the Cubic Law is proposed to commonly describe the Darcy linear flow through the parallel-plates with constant aperture:

$$-\nabla P = -\frac{\mu Q}{k_0 e_h w} \tag{3}$$

where  $Q [L^3 T^{-1}]$  is the flow rate, and  $\nabla P [ML^{-2} T^{-2}]$  is the hydraulic pressure gradient.  $e_h [L]$  is the hydraulic aperture and  $w$  is the asperity of the fracture,  $\mu [ML^{-1} T^{-1}]$  is the dynamic viscosity of the fluid,  $k_0 [L^2]$  is the fracture permeability.

However, for the flow through the complicated geometries of the 3D real rough rock fracture, the inertial effect may become significant even at a low Reynolds number, especially under increasing confine stresses (Zhou et al. 2015). For these situations, the ignorance of the acceleration terms may overestimate the flow rates and result in deviations from reality, further causing the occurrence of the non-Darcy flow in

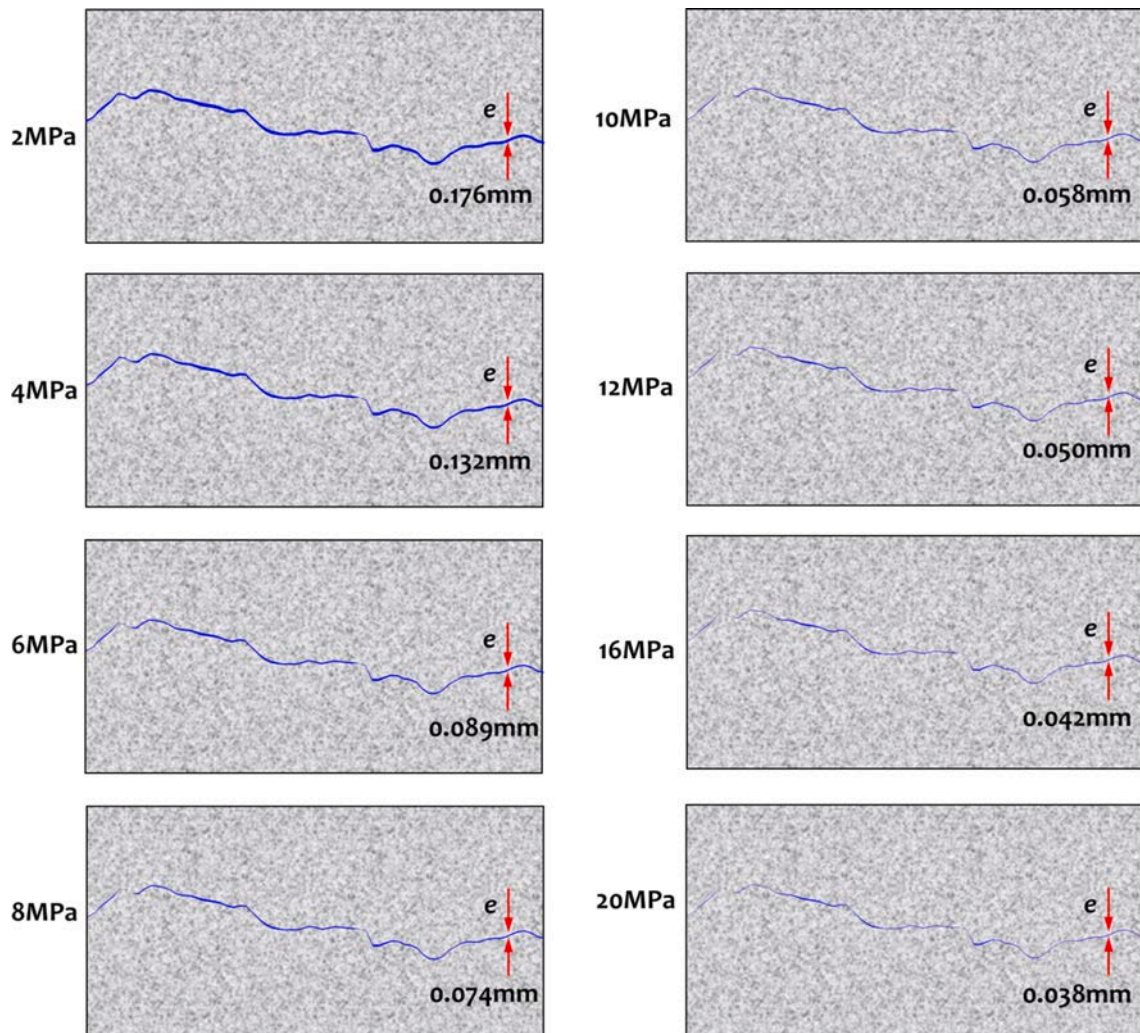


Fig. 6. Illustration of the fracture aperture variation with the increasing confine stresses.

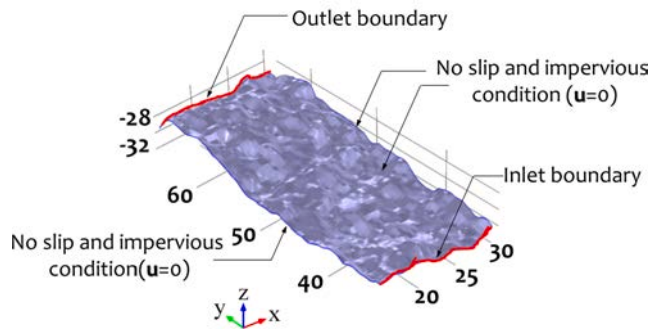


Fig. 7. Boundary conditions for the flow model.

fractures, which is widely characterized by the zero-intercept quadratic equation proposed by Forchheimer (1901):

$$-\nabla P = A Q + B Q^2 \quad (4)$$

where  $A$  [ $ML^{-5}T^{-1}$ ] is the coefficient of the linear term, representing the water pressure losses due to viscous dissipation mechanisms, and  $B$  [ $ML^{-8}$ ] is the coefficient of the non-linear term, describing the pressure losses caused by the inertial effect (Javadi et al. 2014). Both coefficients  $A$  and  $B$  depend on the fluid properties and the geometric characteristics of rough fractures (Chen et al. 2015):

$$A = \frac{\mu}{kA_h} = \frac{12\mu}{we_h^3} \quad (5a)$$

$$B = \frac{\beta\rho}{A_h^2} = \frac{\beta\rho}{w^2e_h^2} \quad (5b)$$

where  $\beta[L^{-1}]$  is the non-linear coefficient, which is related to the geometric characteristics of fractures. To consider the inertial effects on flow capacity through the fracture, Eq. (4) can also be written as:

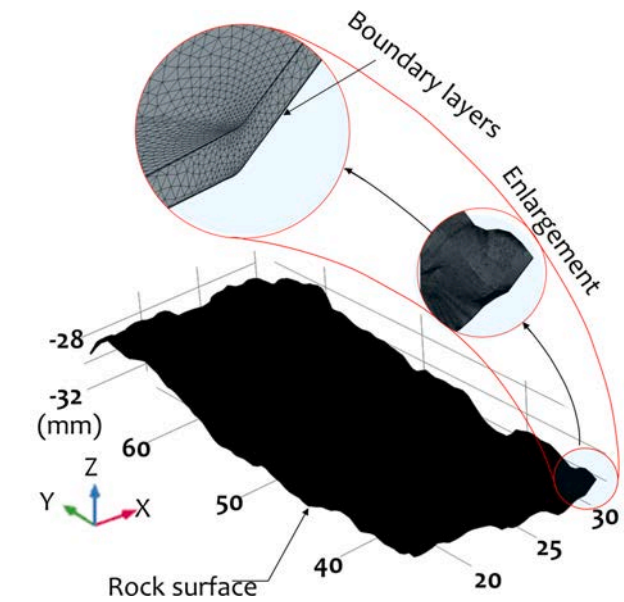


Fig. 8. Tetrahedral control mesh of the rough fracture using COMSOL™, the enlarged circles show the meshing clearly.

$$-\nabla P = -\frac{\mu Q}{k_0 e_h w} (1 + F_0) \quad (6)$$

where  $F_0 = \frac{\beta Re_{ch}}{12}$ , is the Forchheimer number, which is related to the fracture geometries and flow velocity. More discussion of  $F_0$  can be obtained from the authors' previous work (Chen et al. 2019). Here, the apparent transmissivity  $T_a = \frac{k_0}{(1+F_0)}$  was used to describe the permeability of the flow in fractures considered inertial effects.

In addition, a key parameter in non-Darcy flow is the Reynolds

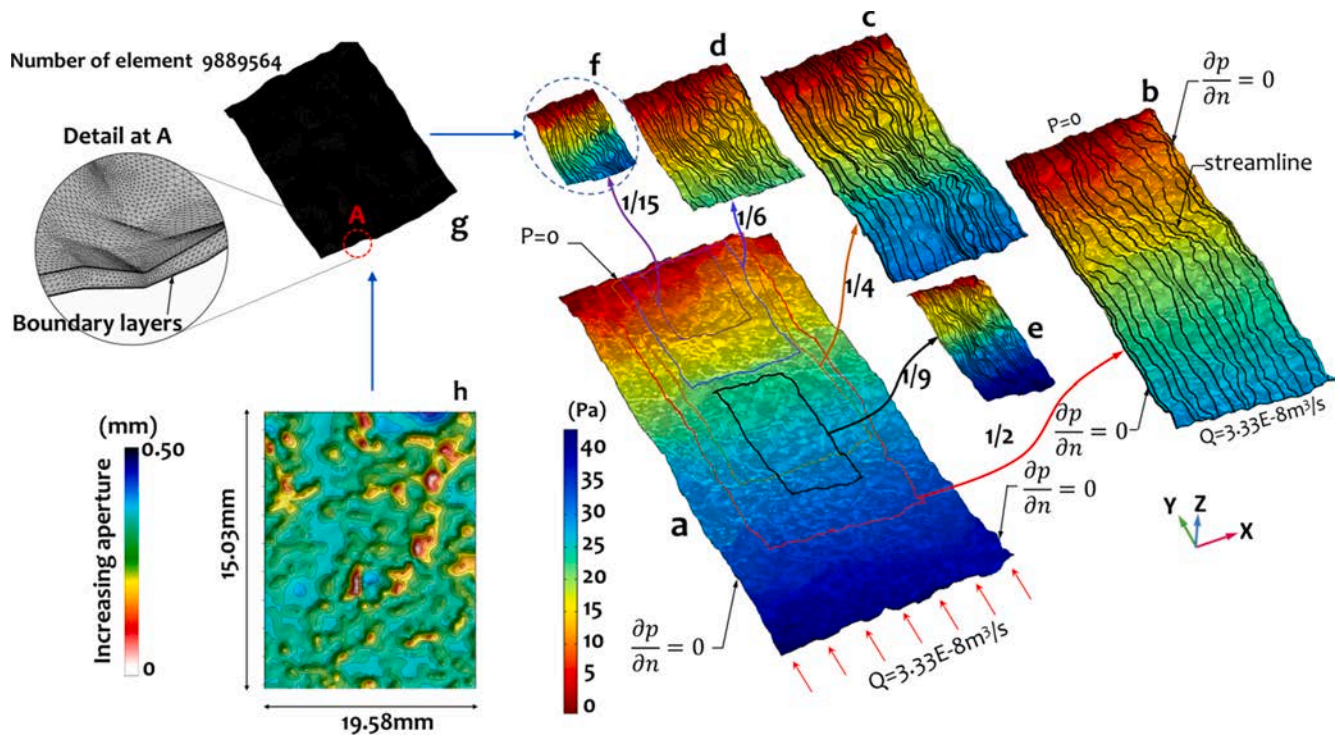


Fig. 9. Flow simulations for various scales of portions of the whole fracture. Figures a-f represent water pressure distribution for different scales of the fracture models cut from the fracture. The injection rate  $3.33E-8 \text{ m}^3/\text{s}$  was the same for all models, and so were the boundary conditions. Figure g is the meshing of the model f. Figure h is the aperture distribution of model f, and the increasing aperture size is represented by white through blue.

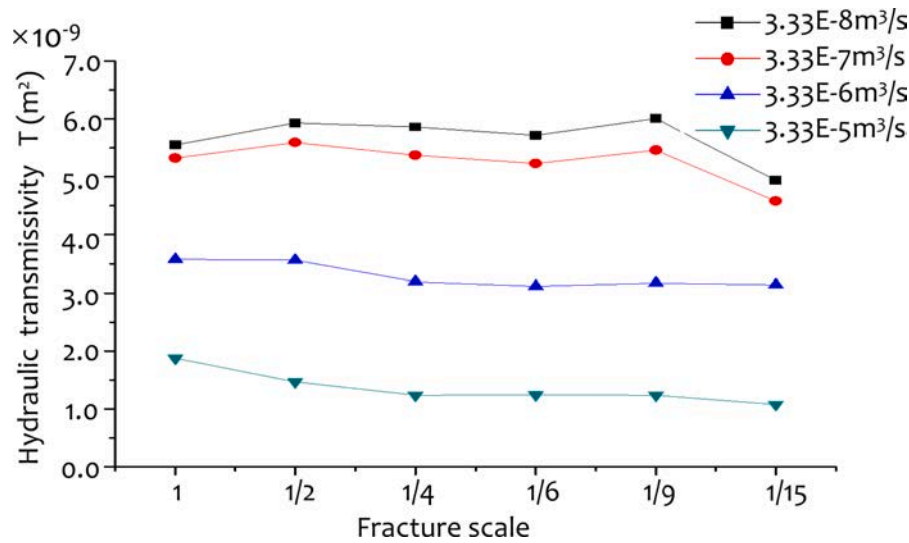


Fig 10. Apparent transmissivity changes with the scales of segments of the fracture under different injection flow rates from 3.33E-8 m<sup>3</sup>/s to 3.33E-5 m<sup>3</sup>/s.

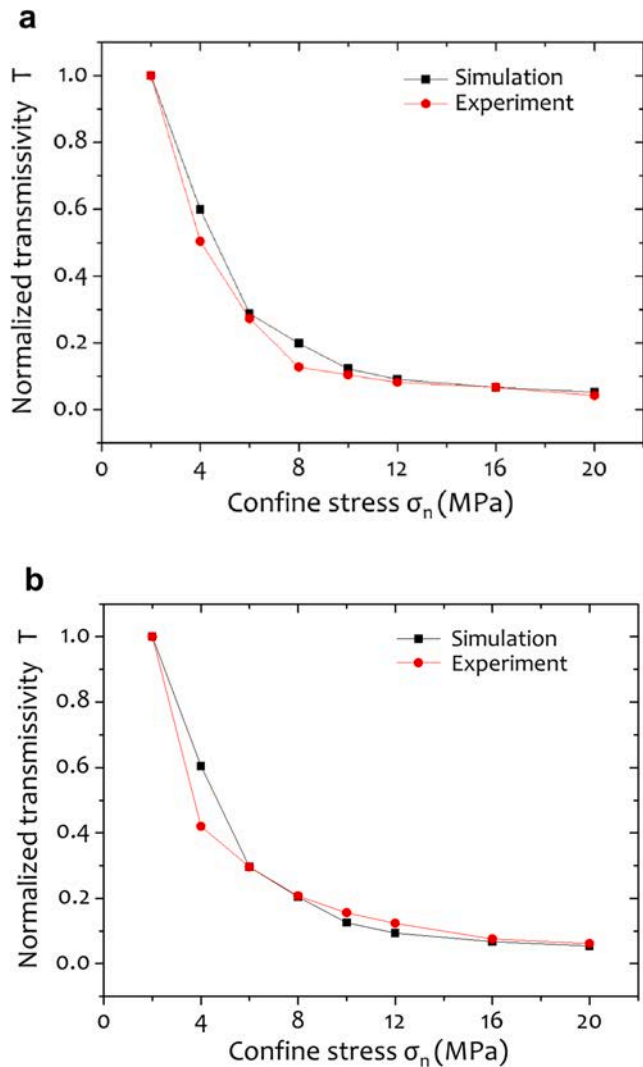


Fig. 11. Comparison of the normalized experimented and simulated apparent transmissivity varies with the confine stress under the inflow rates of 3.33E-8 m<sup>3</sup>/ (a) and 3.33E-7 m<sup>3</sup>/s (b).

number  $Re$ , which is defined as the ratio of the inertial force to the viscous force (Javadi et al. 2014):

$$Re = \frac{\rho Q}{\mu w} \quad (7)$$

According to Eq. (7), the Reynolds number  $Re$  increase with the flow rate. When the Reynolds number exceeds a critical value, i.e. critical Reynolds number, the non-Darcy flow behavior will gradually appear. With regard to the non-Darcy flow in fractures described with Forchheimer's law (Eq.(4)), the onset of transition from linear to non-Darcy flow can also be reflected by the non-Darcy effect factor  $E$ , defined as (Rong et al. 2016):

$$E = \frac{BQ}{A + BQ} \quad (8)$$

It can be found that  $E$  is the ratio of pressure gradient dissipated by the nonlinear effect over the total pressure gradient (Zhang and Nemcik 2013; Zhou et al. 2015), with the physical interpretation of the degree to which the fluid deviates from the linear flow.

Combining Eqs. (5), (7) and (8), the Reynolds number  $Re$  is rewritten as:

$$Re = \frac{A\rho E}{B\mu w(1 - E)} = \frac{12E}{\beta e_h(1 - E)} \quad (9)$$

Eq. (9) is the expression of the Reynolds number commonly used for non-Darcy flow in rough fractures. It can be seen that  $Re$  is determined by the non-Darcy effect factor  $E$ , and the geometric characteristics of the fracture, including the non-Darcy coefficient  $\beta$  and the hydraulic aperture  $e_h$ .

### 3. Flow simulations in 3D rough rock fracture

To model the flow characteristics in 3D single rough rock fracture with geometry changes under confine stresses, the first step is to determine the variable fracture geometries subjected to increasing confine stresses based on experimental measurements.

#### 3.1. Test measurement observations

##### 1) Measurement I — Hydraulic tests

The tunnel excavation induced rock fractures formed in the

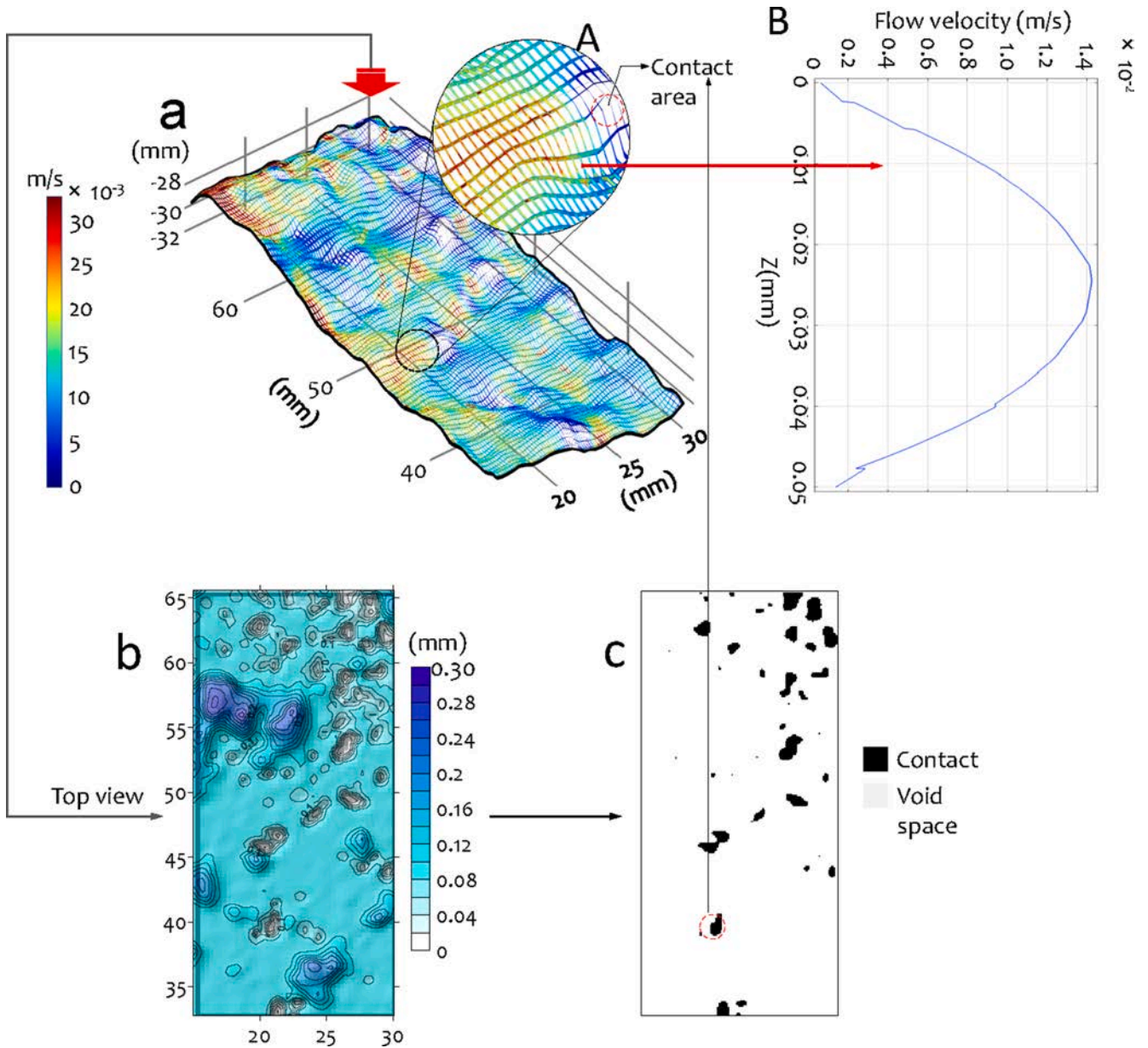


Fig. 12. (a) Flow velocity fields for the fluid flow along the axis of the specimen under a confine stress of 6 MPa and injection rate of  $3.33E-8 \text{ m}^3/\text{s}$  ( $Re = 2.22$ ), (b) The contact areas and aperture distributions in the rough fracture. (c) Spatial distribution of contact areas (black) and apertures (white).

surrounding sandstone strata are the main channels of groundwater inflow toward the excavation faces (Chen et al. 2018), and the redistribution of the excavation-induced stress result in the deformation of a rock fracture and further affect groundwater inflow. A cylindrical sandstone specimen with the size of  $50 \text{ mm} \times 100 \text{ mm}$  was prepared by coring a large sandstone block obtained from the Permian Carboniferous strata in Shanxi Province. Using the Brazilian tensile test, a single rough fracture located along a diametral plane was experimentally produced (Fig. 2). A servo-controlled tri-axial system was adopted to conduct hydraulic tests through the rough fracture subjected to various levels of radially applied confine stresses (Fig. 3-a). The test system contains the triaxial cell ( $\leq 70 \text{ MPa}$ ), the servo-controlled axial and circumferential loading system. A high-precision hydraulic pump with maximum water pressure and injection rate being 20 MPa and 40 m/min, respectively, was used. A high-precision electronic balance with the precision of 0.0001 g was placed at the outlet for measuring the flow rate (Fig. 3-a).

The data acquisition system was used to record all measured data in real-time. The test procedures were briefly described below.

Firstly, the fractured samples were saturated for 24 h under the vacuum condition, then taken out and twined around by PVC adhesive tape and enclosed in the heat-shrinkable sleeve for sealing. Subsequently, two porous plates are placed onto two ends of the sample to ensure the even distribution of water pressure over each end. The sleeve-enclosed sample was fixed between the base pedestal and top cape using the iron wire and then installed in the tri-axial cell (Fig. 3-a). The increasing confine stresses were applied by using the servo-controlled circumferential system to change the apertures of the fracture sample. At each confine stress level, unidirectional fluid flow tests were conducted by increasing flow rates from 1 ml/min to a maximum of about 30 ml/min. The fluid was injected into the lower end of the sample, and these tests were performed to investigate how the fluid flow behavior changed with the variable apertures under confine stresses ranged from

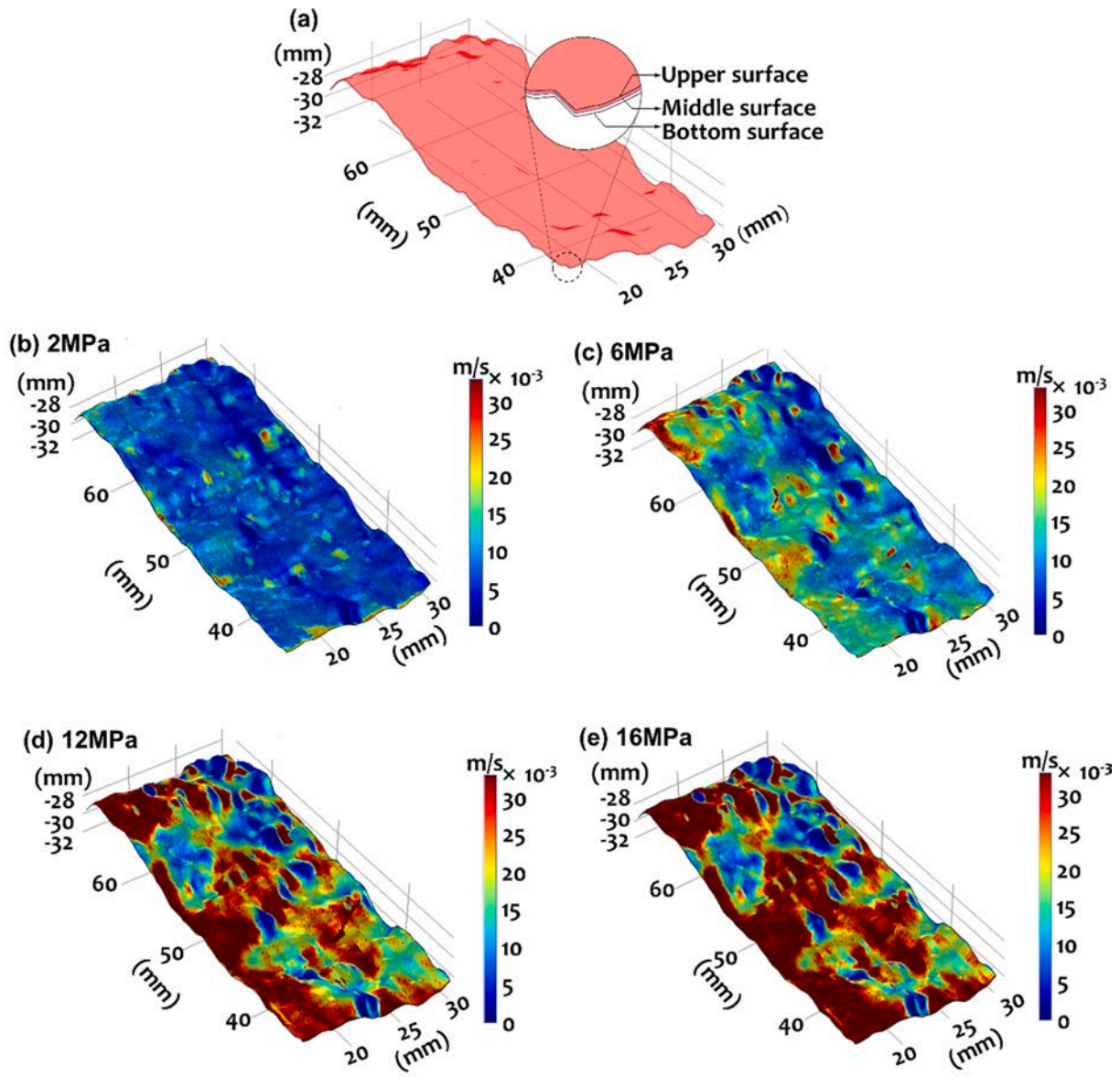


Fig. 13. Flow velocity fields of the specimen at the middle fracture surface at an injection flow rate of  $3.33\text{E-}8 \text{ m}^3/\text{s}$  ( $Re = 2.22$ ) under different mechanical apertures. (a) Schematic diagram of the middle surface. (b)–(e) Flow velocity fields under different apertures conditions. Zones where the velocity was larger than  $0.03 \text{ m/s}$  are all shown in red.

0 to 20 MPa. Two radial displacement extensometers were installed normal to the fracture surface of the sample to measure the fractured rock deformation under increasing confine stresses (Fig. 3-b&c). In addition, two fracture surfaces were sprayed with a thin layer of the developer (dye penetrant supplied by Inspection Equipment Co. LTD, Shanghai) that could easily be washed away by the fluid flow; this allowed a clear observation of the flow path (shown in Fig. 2-b). The flow test data is used to validate the following simulation results, and it will be represented in Section 3.1.

2) Measurement II — Fracture aperture characterization

The fracture apertures, i.e. the spatial positions of the upper and lower fracture surfaces, are necessary to develop the 3D real fracture model. Here, the point-cloud matching method is used to measure the fracture apertures at the initial zero stress condition (Chen et al. 2017), and the measurement procedures are described below (Fig. 4):

- 1) Through scanning the locating points attached to the rock ends by using 3D scanner (OKIO-H-200, TENYOUN), the spatial coordinates system  $P_{\text{ext}}$  of exterior surfaces of the sample was captured to serve as a reference position. The fractured sample was open and the spatial coordinates of exterior surface  $P_{\text{ext}}$  and that of fracture surface  $P_{\text{surf}}$  of each block in current spatial coordinate system were obtained.
- 2) By matching  $P_{\text{ext}}$  and  $P_{\text{surf}}$ , a coordinate transformation can be made to obtain  $P_{\text{surf}}$  from  $P_{\text{surf}}$ . That is why we call the approach “point cloud data matching method”.

Then the matched point-cloud data of the upper and lower fracture surfaces were converted to a high-precision discrete mesh using the Kriging gridding method. The grid intervals in x- and y- directions are  $0.01 \text{ mm}$  for two meshes. The fracture aperture  $E_{\text{ini}}^i$  at any grid point  $i$  in the initial zero stress state can then be calculated by:

$$E_{\text{ini}}^i = z_u^i - z_l^i \tag{10}$$

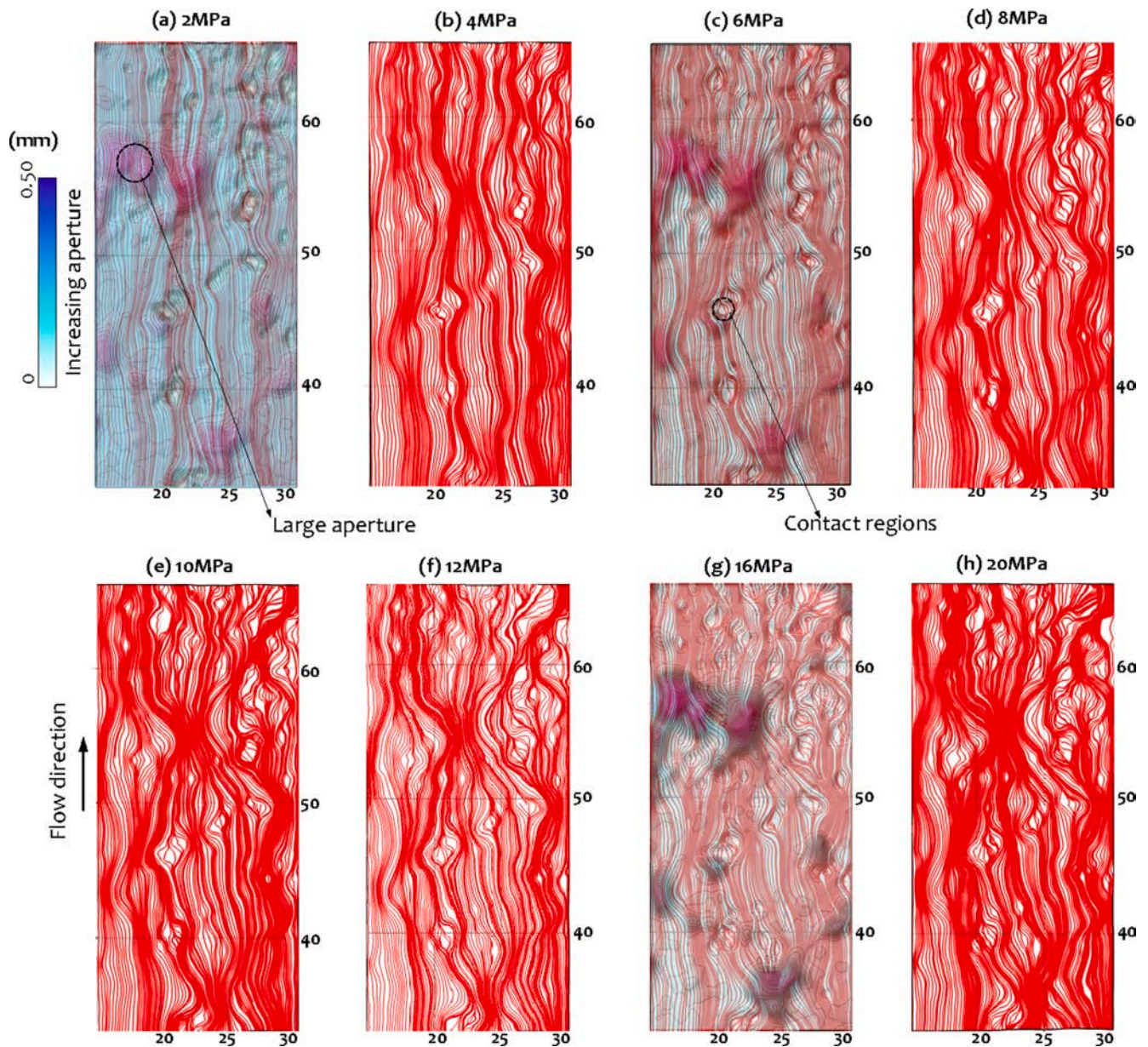


Fig. 14. Top view of evolutions of streamlines in 3D rough fracture models under an injection flow rate of  $3.33\text{E-}8 \text{ m}^3/\text{s}$  ( $Re = 2.22$ ) and the increasing confine stresses from 2 MPa to 20 MPa.

where  $z_u^i$  and  $z_l^i$  represent the Z-elevation of the point  $i$  at the upper and lower fracture surfaces, respectively. After obtaining the fracture aperture, the contact area, defined as fracture apertures below  $10 \mu\text{m}$  (limited by the scanning precision of  $10 \mu\text{m}$ ), can be determined, while the remaining fracture apertures, greater than  $10 \mu\text{m}$ , are regarded as void spaces (Chen et al. 2017). After obtaining the measured 3D fracture morphology data at zero stress state, the stress induced alteration in apertures, including void spaces and contact distributions, within the fracture can be determined, as described below, which is necessary to investigate the geometry characteristics of the 3D real rough fracture.

### 3) Measurement III — Stress induced aperture variations

In general, the deformation behavior of rock fracture is a complicated process and is difficult to be introduced into the modeling. To experimentally obtain the fracture deformation rather than through any

empirical relations or contact models, some assumptions for the closure of fracture aperture resulting from a change in stress normal to the fracture is depicted as follows based on above test measurements:

- 1) The fracture closure is accommodated only by the compression of the surface asperities on either side of the fracture plane that is in contact with each other, conforming to the “bed of nails” model (Gangi 1978; Tsang and Witherspoon 1981)
- 2) The measured fracture closure due to the confine loading is distributed uniformly over the whole fracture surface, resulting in the same change in the aperture at any location;
- 3) Overlapping asperities are assumed to be contacting asperities, and the fracture surface deformation was not considered due to its little influence on fluid flow characteristics (Brown 1989; Ishibashi et al. 2015).

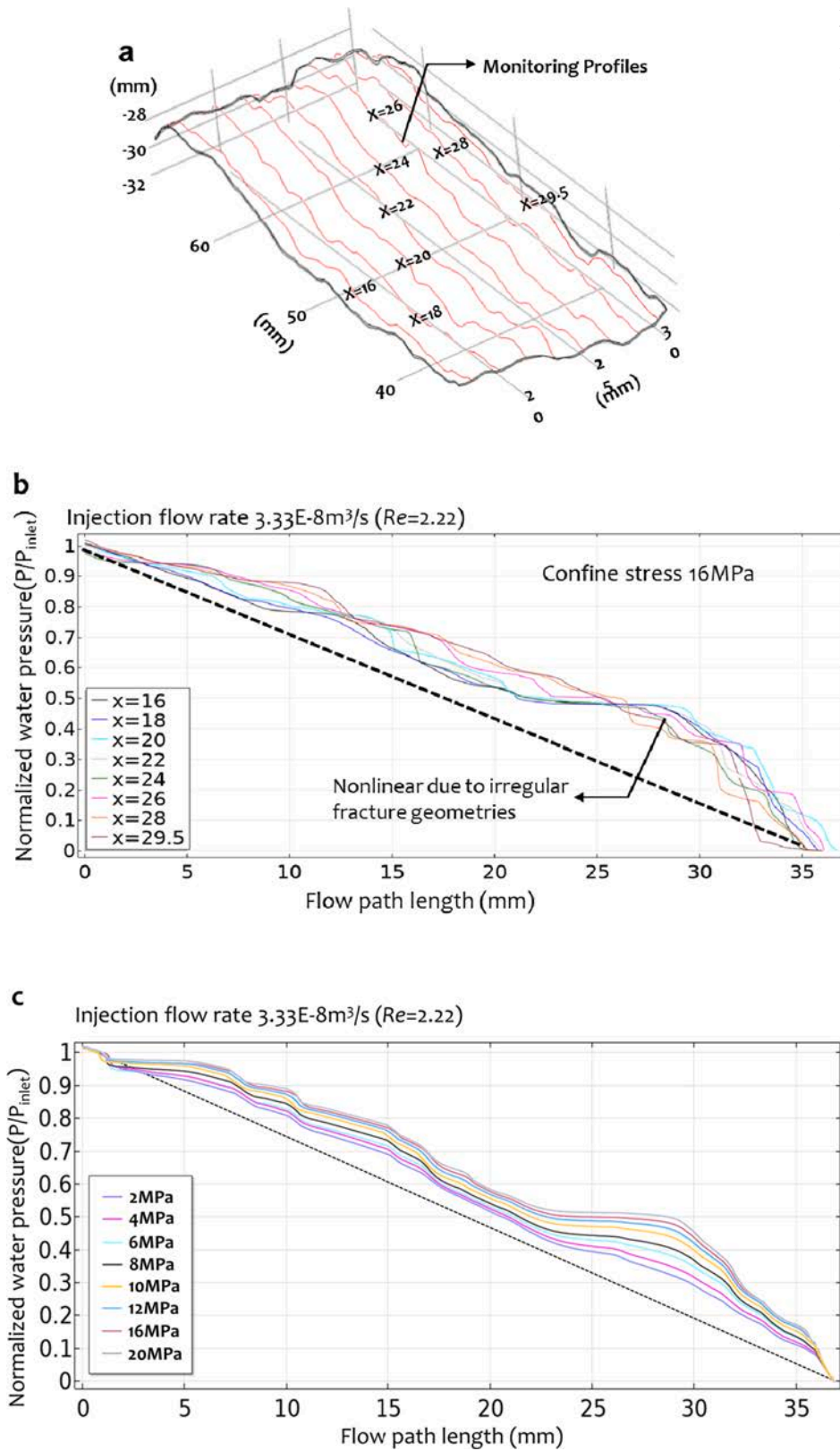


**Fig. 15.** (a) Locations of the monitoring lines parallel with the y-axis of the fracture in the middle surface of the rough fracture, (b) water pressure decrease nonlinearly along the different profiles under the confine stress 16 MPa and injection flow rate of  $3.33E-8 m^3/s$  ( $Re = 2.22$ ), (c) water pressure decrease nonlinearly along the profile X = 24 under different confine stress and injection flow rate of  $3.33E-8 m^3/s$  ( $Re = 2.22$ ), (d) water pressure decrease along the profile X = 24 under different confine stress and injection flow rate of  $3.33E-5 m^3/s$  ( $Re = 2220$ ).

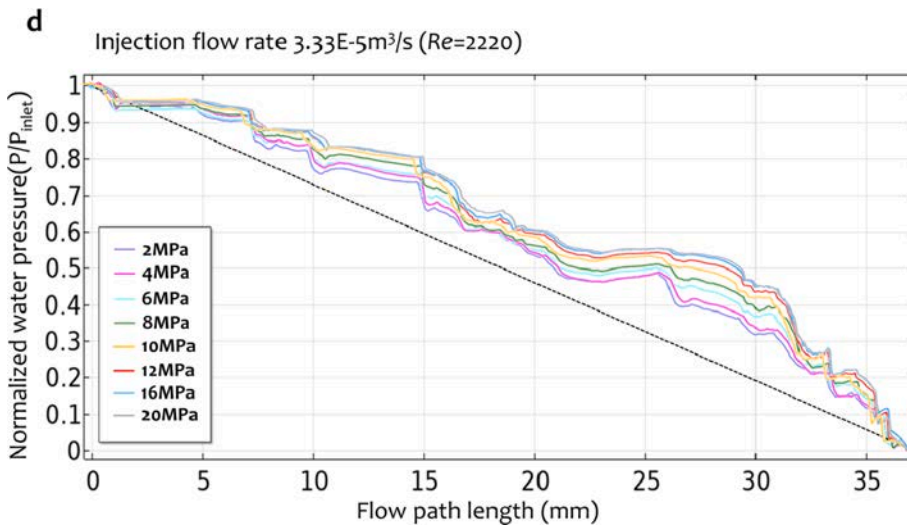


Fig. 15. (continued).

Based on the above mechanism, the fracture aperture ( $E_{ini}$ ) at the zero-stress condition minus the measured average fracture deformation ( $\Delta E_n$ ) serves the basis to obtain the fracture aperture ( $E$ ) under different stresses:

$$E = E_{ini} - \Delta E_n \quad (11)$$

Here, the average fracture deformation is regarded as the difference of the displacement between the fractured and intact rock deformation measured using the radial extensometers at different stress levels (Fig. 5). The principle of this method is in accordance with many laboratory studies (Raven and Gale 1985; Renshaw 1995; Selvadurai 2015). The test measured fracture apertures change due to the changing confine stress were given in Fig. 5. Based on the results, the void spaces and contact distributions within the fracture under increasing confine stress can be determined experimentally.

### 3.2. Model setup

The rough fracture surfaces can be duplicated in the model using the high-precision *parameterized surface* functions in the COMSOL<sup>TM</sup> software. The irregular spatial structure sandwiched between two parameterized surfaces, built based on two fracture surfaces, can be employed to represent the real fracture geometries in three-dimensions. In the modeling, due to the restricted precision of the geometric reconstruction and the computational cost using COMSOL<sup>TM</sup>, two reasonable simplifications for the flow simulations were proposed below.

Firstly, the contact areas between two parameterized surfaces that possess zero values for the aperture can easily cause unavoidable geometric errors and obstruct the subsequent steps, including the mesh generation and flow calculations. Such errors are not seen in the geometric modeling of small-scale fracture surfaces but become more pronounced as the scale increases. Thus, to avoid such errors, a special treatment that assigns very small aperture values (about 10  $\mu\text{m}$ ) to the contact elements was adopted.

Secondly, the simulations of the problem were limited by the computational capacity to solve the NS equation for whole 3D fracture geometry with an extremely fine meshing representation, especially for tiny apertures under high confine stress. Since the hydraulic transmissivity was proved to be independent of the scales of the fracture

models within limits (Related discussion was provided in Section 3.1), to reduce the computational cost, a scale of 1/9 of the entire fracture,  $x = [15, 30]$  mm and  $y = [32.8, 65.6]$  mm, was chosen to form the 3D models for flow simulations in this study.

In the modeling, the Navier-Stokes equations Eqs. (1) and (2) were solved using COMSOL Multiphysics software. Since the study focuses on how changes in contact regions and void spaces in 3D real rough fractures affect final stabilized flow behavior in fractures, changes in the flow characteristics over time are not a consideration, allowing the steady solver to be used instead of the transient solver. Besides, the hydro-mechanical coupling model was not considered due to research limitation and more related information can be referred to Jia et al. (2020). The density and viscosity coefficient of water are set to 1000  $\text{kg}/\text{m}^3$  and  $1 \times 10^{-3}$  Pa·s, respectively.

### 3.3. Boundaries conditions and simulation procedures

Based on the above reasonable simplifications, the fracture morphologies, measured under different confine stresses of 2 MPa, 4 MPa, 6 MPa, 8 MPa, 10 MPa, 12 MPa, 16 MPa, and 20 MPa were used to build the 3D real fracture models (Fig. 6).

Once the geometry of the model was completed, it is straightforward to assign the suitable initial and boundary conditions for the flow simulation in COMSOL<sup>TM</sup>. At each fracture model, four injection flow rates, from  $3.33\text{E-}8$   $\text{m}^3/\text{s}$  to  $3.33\text{E-}5$   $\text{m}^3/\text{s}$ , corresponding to Reynolds numbers ( $Re$ ) from 2.22 to 2220, were kept constant along the inlet boundary at  $y = 0$  mm and zero pressure, i.e.  $P = 0$ , along the outlet boundary (Fig. 7), to investigate the flow behavior variations in a rough fracture caused by the effects of injection rates and the compression stresses. The upper and lower fracture surfaces and the side boundaries in the fracture model were specified as impervious, i.e.  $\partial h/\partial n = (\nabla h) \cdot \mathbf{n}$  and non-slip boundaries, i.e.  $\mathbf{u} = 0$  m/s. Such boundary conditions are consistent with several laboratory experiments (Chen et al. 2017; Zhang and Nemeik 2013; Develi and Babadagli 2015; Zou et al. 2017a; 2017b). To reduce the boundary effects, a laminar entrance inflow condition provided by COMSOL was adopted in all simulations (Zou et al. 2017b).

The tetrahedral elements, which provide flexibility to accommodate complex irregular geometries that have finer meshes around the small apertures, were used. The representative of the discretization of the

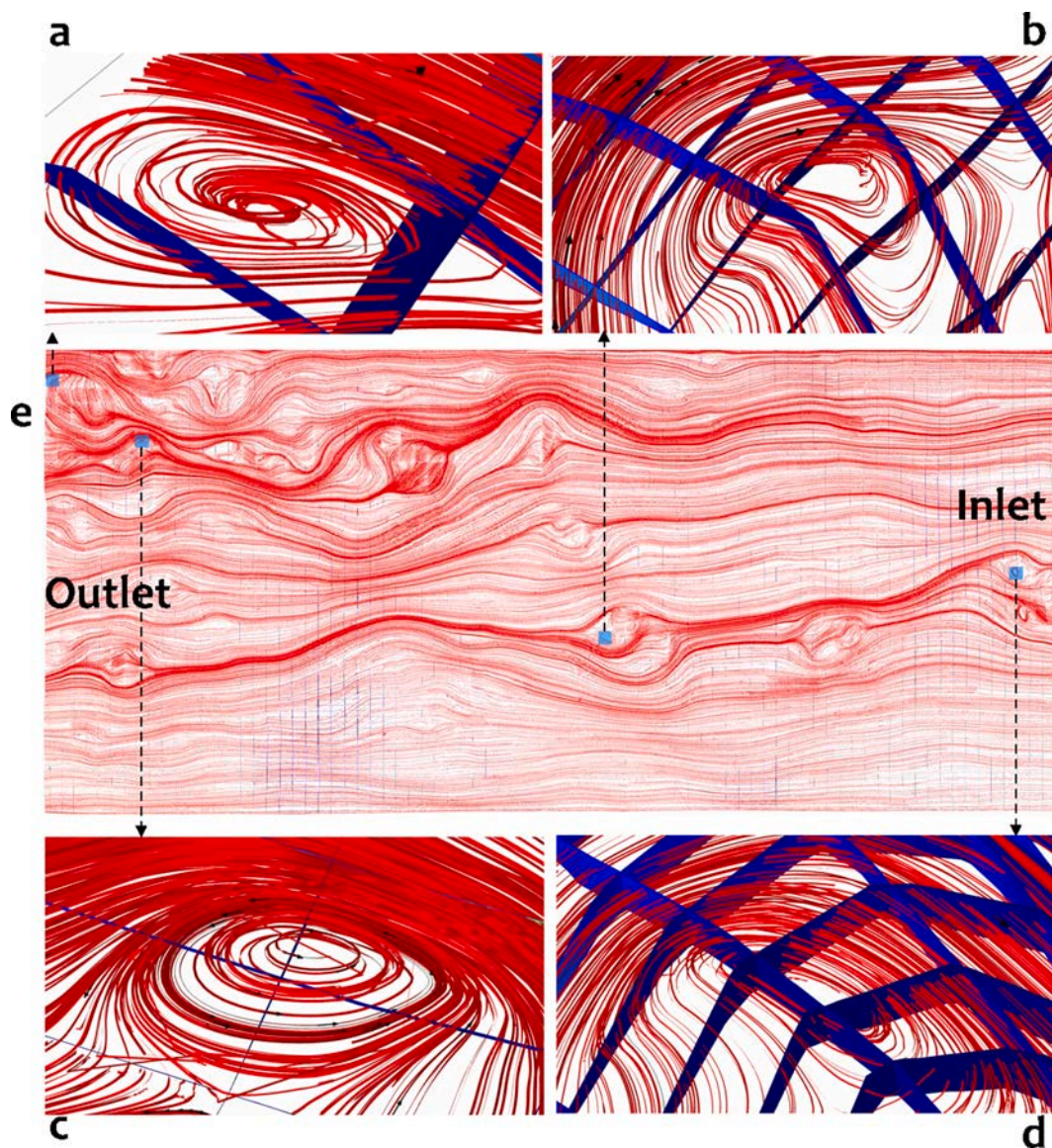


Fig. 16. The enlarged view of flow streamlines in different small-scale region (a, b, c, d) in 3D real rock fracture (e) under the confine stress 10 MPa and injection flow rates  $3.33E-5 \text{ m}^3/\text{s}$  ( $Re = 2220$ ).

fracture is presented in Fig. 8. A sensitivity analysis was conducted to examine the influence of increasing grid numbers on the flow behaviors under the confine stress of 10 MPa and a flow rate of  $3.33E-8 \text{ m}^3/\text{s}$  ( $Re = 2.22$ ). The results show that the pressure drop between the injection and outlet ends keeps almost constant with an increase in grid numbers from 13.7 million to 20.2 million tetrahedral elements. The combinations of eight confine stress and four injection velocities result in 32 modeling cases.

## 4. Results

### 4.1. Modeling validation with test results

To verify the rationality of choosing the small-scale fracture model for flow simulations, a series of different scales of fracture models chosen from the whole fracture were conducted for flow simulations (Fig. 9). The apparent transmissivity change with the scales of the fractures under different injection rates is shown in Fig. 10. The transmissivity fluctuates in a tight range when the scale changes from 1 to 1/9 and then drops sharply as the scale decrease to 1/15, indicating the

transmissivity is independent of the scales of the fracture models within limits. Thus, the simulation results of the model with the scale of 1/9 of the entire fracture are available to characterize that of the whole rock fracture, which is reasonable to compare with test results.

Since the inflow rates of  $3.33E-6 \text{ m}^3$  and  $3.33E-5 \text{ m}^3$  were not applied in the hydraulic tests, the normalized simulated and measured apparent transmissivity, at the inflow rates of  $3.33E-8 \text{ m}^3/\text{s}$  and  $3.33E-7 \text{ m}^3/\text{s}$ , respectively, were compared in Fig. 11.

Here, the injection flow rate  $3.33E-8 \text{ m}^3/\text{s}$  and  $3.33E-7 \text{ m}^3/\text{s}$  used in flow simulations equal to 2 ml/min and 20 ml/min that applied in tests. The normalized apparent transmissivity refers to the ratio of the monitored apparent transmissivity to the apparent transmissivity at the low confine stress of 2 MPa. It shows that both the measured and simulated transmissivity decreases exponentially with the increase in confine stresses, and the simulation values match well with that measured at each stress level, under the inflow rates of  $3.33E-8 \text{ m}^3/\text{s}$  and  $3.33E-7 \text{ m}^3/\text{s}$ , respectively, indicating that the flow simulations using N-S equations can well describe the flow capacity in 3D real rough fractures subjected to the confine stress. This provides a basis for the following representation of the flow characteristics within the rock fractures under

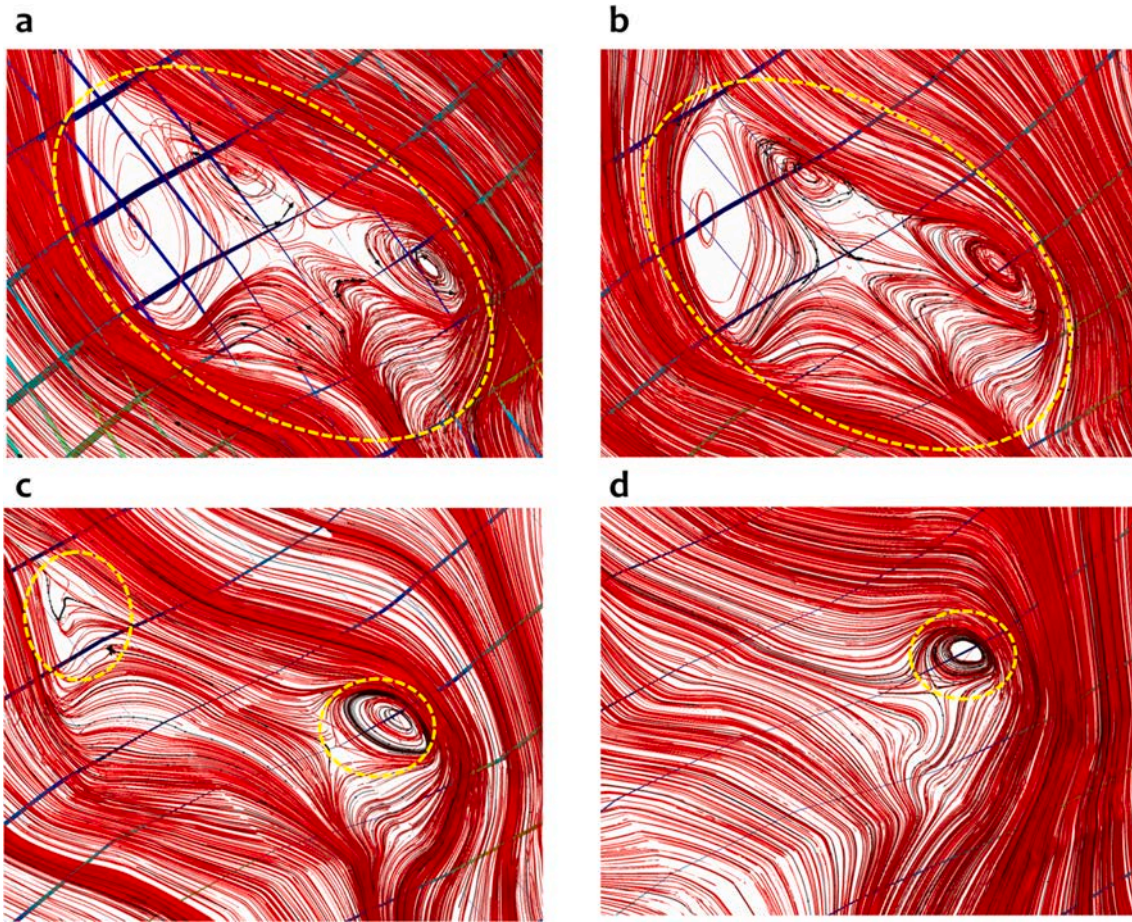


Fig. 17. Variation of range of the eddy flow occur within the same region in the rough fracture under different confine stresses, 2 MPa (a), 6 MPa (b), 10 MPa (c) and 20 MPa (d) and the flow rate of  $3.33E-5 \text{ m}^3/\text{s}$  ( $Re = 2220$ ).

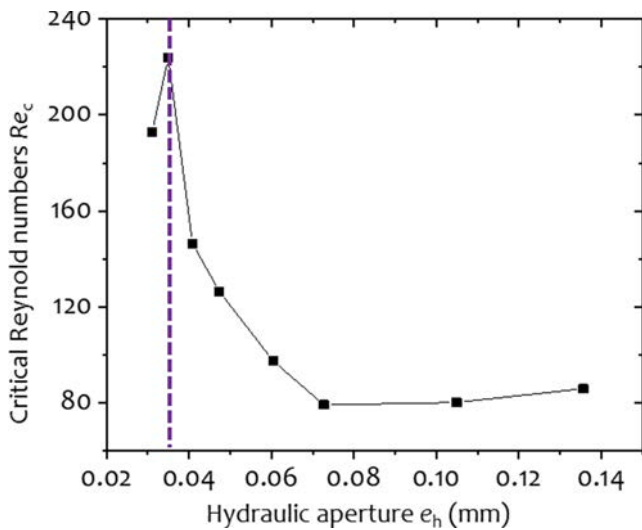


Fig. 18. Variation of  $Re_c$  with the hydraulic aperture  $e_h$  for the 3D real rough fractures.

the high confine stress, including the distribution of velocities, streamlines, as well as the inner water pressure, which cannot be easily observed in tests.

#### 4.2. Flow behaviors characterizations

Fig. 12-a shows the norm of the flow velocity magnitude field,  $U = \sqrt{u_x^2 + u_y^2 + u_z^2}$ , in sectional views of the  $x$ - and  $y$ - directions, for the confine stress of 6 MPa and injection flow rate of  $3.33E-8 \text{ m}^3/\text{s}$  ( $Re = 2.22$ ), which was distributed non-uniformly at the surface due to the void spaces and asperity contact alterations. It was widely reported in previous research that the flow velocity through a small aperture is larger than that of a large aperture in 2D models due to the mass conservation law (Koyama et al. 2008; Zhang et al. 2015). However, in the 3D model, high-velocity zones (red areas) appear in large apertures and their locations dependent on the spatial distribution of the contact areas (black) and apertures (white) shown in Fig. 12-c, where apertures of less than or greater than  $10 \mu\text{m}$  are marked with black and white, respectively. The distribution of apertures in the fracture is shown in Fig. 12-b. The flow velocity through each aperture, shown in the enlarged views A and B of Fig. 12-a, trends to zero along the upper and lower fracture walls due to the no-slip effects and reaches its maximum value in the mid-plane. These characteristic variations in fluid flow conform to the well-known Poiseuille flow with a parabolic velocity profile across the fracture aperture (Kundu and Cohen 2008). Thus, to more clearly

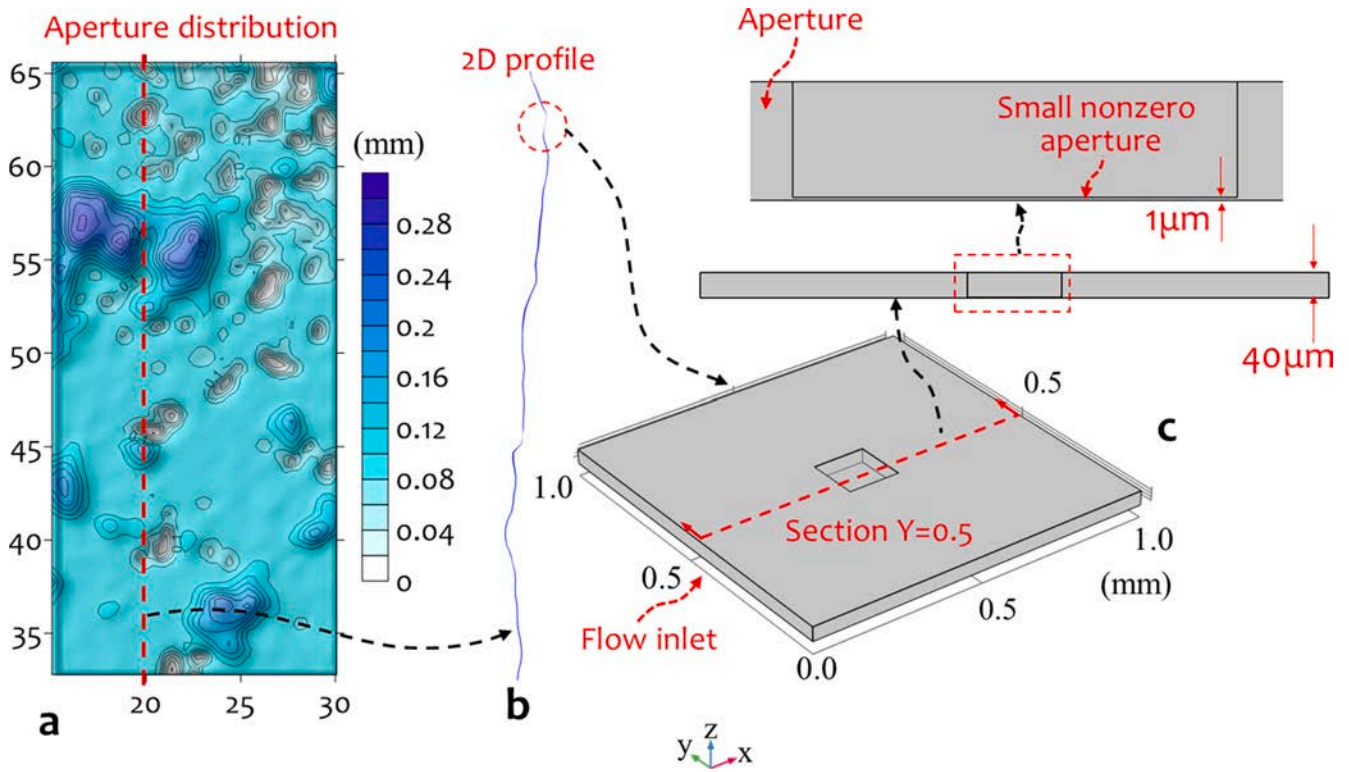


Fig. 19. A simplified 3D representative model with a regular shape built from the rock fracture, (a) Aperture distribution of the fracture, (b) 2D surface profile, (c) idealized cubic model including both the contact (nonzero small aperture 1 μm) and aperture.

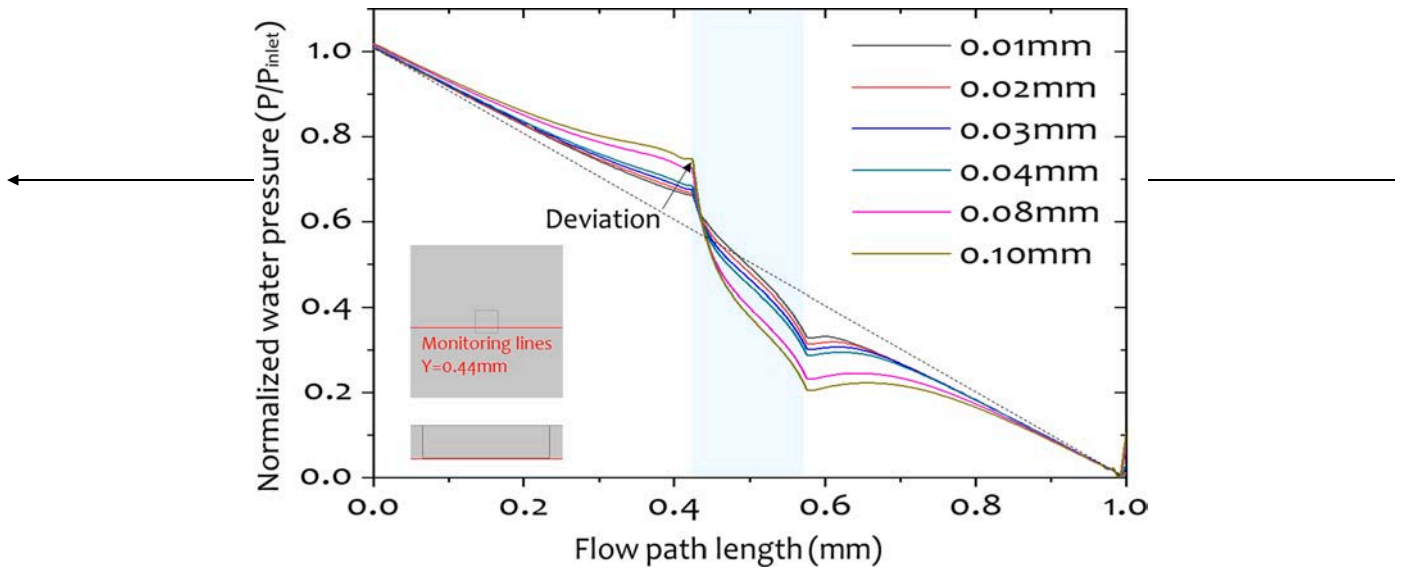
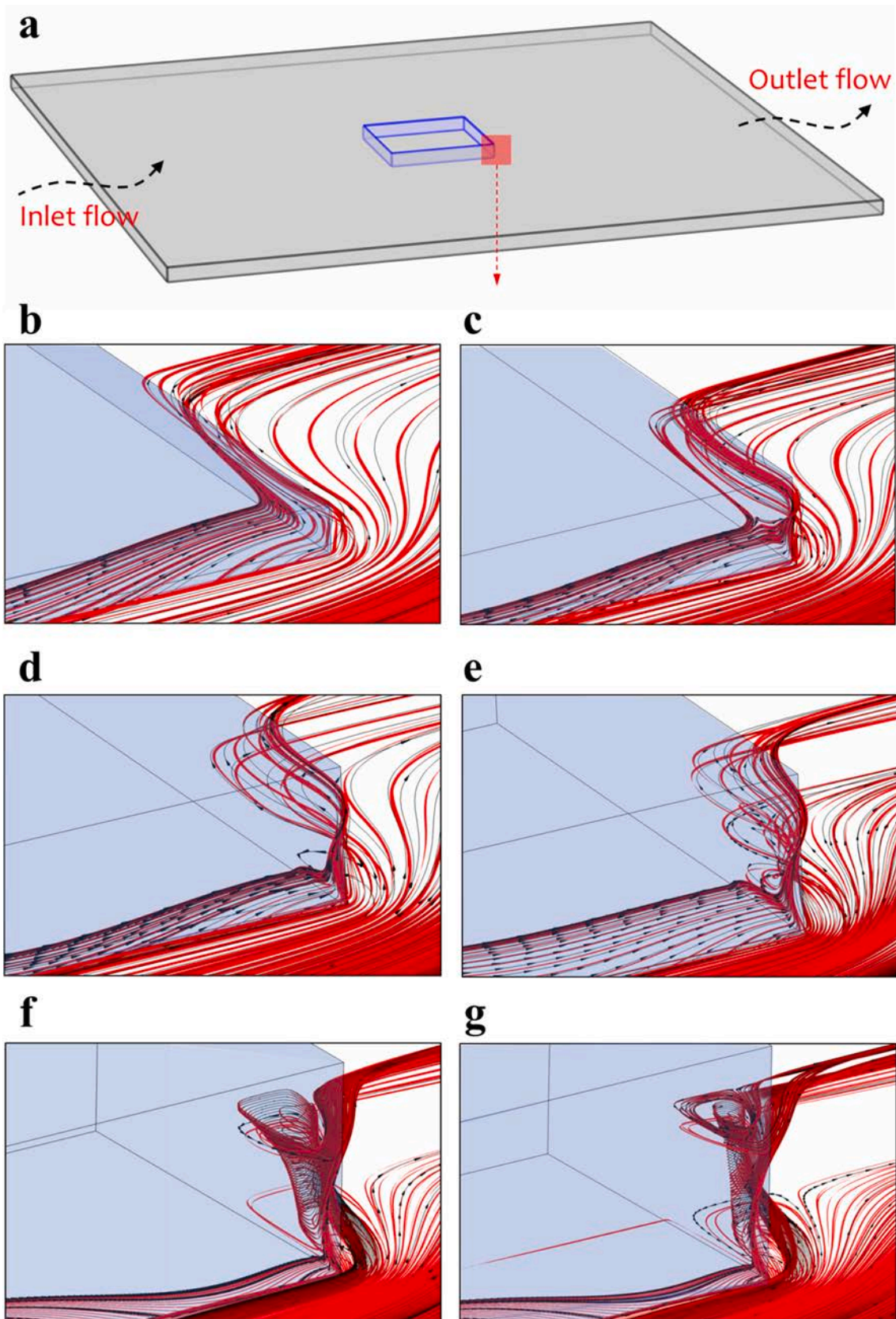


Fig. 20. The water pressure decreases along the monitoring line  $Y = 0.44$  mm located close to the bottom of the model,  $Z = 0.0005$  mm, for different fracture apertures.



**Fig. 21.** Variation of the streamlines occur at the corner of the contact for different fracture apertures, (b)–(f) indicates the different cases of the aperture increase from 0.01 mm to 0.1 mm. (The streamlines around the corner are only presented for clear illustration).

characterize the variations of fluid flow velocities in rough fractures with confine stresses, the contour maps representing the values of flow velocities at the mid-surface of the fracture are given in Fig. 13. The results show that the flow velocity  $U$  under higher confine stresses was distributed more non-uniformly than under low-stress conditions, due to the more heterogeneous distribution of aperture and contact under high confine stress.

The changes in the distribution of streamlines at different confine stress are shown in Fig. 14, where the figures (a), (c), and (e) also include the distribution of apertures to indicate that the dense flow lines are mostly concentrated in large apertures. The significant heterogeneity of the streamlines in fractures in these figures clearly illustrate how the water pressure and flow velocity varies with decreasing apertures. At the lower confine stresses of 2 MPa (Fig. 14-a), the streamlines were uniformly distributed along the axial direction of the fracture, with some small-scale tortuosity occurring locally in the contact regions. As the confine stress increases, a more heterogeneous distribution of contact over the entire fracture, blocks the fluid flow. As a result, the streamlines become more channeled with obvious tortuosity, indicating that the locations of the contact areas are the main cause of the deviations in the linear streamlines.

In general, the contact and small apertures could induce higher resistance to flow, and the increase in the heterogeneous distribution of contact due to confine stress causes the non-uniform distribution of the water pressure within the rock fracture. The heterogeneous fluid pressure distributed over rock fracture is observed in experimental, simulation, and field studies (Yeo et al. 1998; Cappa et al. 2019; Ji et al. 2020). To quantitatively represent the distribution of water pressure within rock fractures, the normalized water pressure, referring to the ratio of the monitored inner water pressure  $P$  to the constant injection water pressure  $P_{inlet}$ , was defined, and its variation along different monitoring profiles parallel to the y-axis direction of the middle surface of the rough fracture (Fig. 15-a), under the confine stress of 16 MPa and injection flow rate of  $3.33E-8 \text{ m}^3/\text{s}$  ( $Re = 2.22$ ), are plotted in Fig. 15-b.

The dashed straight lines are provided to illustrate the degree of deviation of the actual pressure decrease from the ideal linear variation. It shows that the pressure decreases non-linearly along these fracture profiles in the rough fracture, indicating that the non-linearity extent of the pressure drop in rock fracture is largely determined by the distribution of contact regions in rock fractures, which bring high water resistance and resulting in the reduced decay of the water pressure. In addition, the variations of normalized water pressure along the profile  $X = 24$  at different confine stresses are plotted in Fig. 15-c. It shows that the degree of non-linearity gradually increases with the confine stress, largely ascribed to the increase of contacts under high confine stress. In addition, with the injection rates increases to  $3.33E-5 \text{ m}^3/\text{s}$  ( $Re = 2220$ ), the overall trends of these curves are unchanged while the local water pressure fluctuated, mainly ascribed to the occurrence of eddy flows formed around contact regions at high flow rates (related mechanism will be discussed in detail below). The non-uniform water pressure in the rough rock fracture is helpful to reveal some geophysical issues, such as the overpressure-induced fracture slip due to the non-uniformly distribution of pore pressure over the fracture plane (Ji et al. 2020), and the resulting heat and mass transport changes.

## 5. Discussion

### 5.1. Non-Darcy flow characteristics in a rough fracture

As the injection rate increases, the eddy flow, which is the main cause of the non-Darcy flow behavior, have caused the apparent inertial effects, resulting in significant fluctuations in the streamlines configuration. These variations in the flow streamlines can be seen more clearly in 3D zoomed-in streamlines in the small regions of the fracture, as shown in Fig. 16. The eddy flow streamlines mostly located around the contact regions (Fig. 16c), or within variable apertures (Fig. 16-a,b,d),

occupying much larger space sizes and showing the closed streamlines with a strong swirling backflow in the horizontal direction and the spiral motion in the vertical direction. The formation mechanism of the complicated streamlines is similar to the typical viscous flow passing around a cylinder column in fluid dynamic (Choi et al. 2008), but with more complicated geometry shapes due to the non-uniform geometry of the contact and apertures (Zou et al. 2017a). These patterns of eddy flows cannot be well represented in the 2D models and not easily observed in lab tests. The results indicate the important effects of geometry changes in 3D rough fracture, which is conformed with the numerical and experimental investigations (Zhang et al. 2013; Lee et al. 2014, 2015; Zou et al. 2017a), in which the contact regions and variable apertures can contribute to obvious eddy flows with an increase in the flow rate, largely due to the inertial effects on the local flow pattern near the voids (Zhang et al. 2013).

In addition, the stress induced change in geometries also significantly affects the patterns of eddy flows in 3D rough fractures. Under the same injection flow rate of  $3.33E-5 \text{ m}^3/\text{s}$  ( $Re = 2220$ ), the range and numbers of the eddy flow occur within the same regions of the rough fracture gradually decreases with the confine stress increasing from 2 MPa to 20 MPa, as shown in yellow circles in Fig. 17 (here the small region in Fig. 16-c was taken to indicate). It clearly shows that, under the low confine stress of 2 MPa, the significant difference of the space size between the contact and the large aperture form the sharp variable geometries, which results in the sharp change of the directions of flow velocity and is conducive to the formation of the eddy flows behind the contact spot. With the confine stress increases, although the increase of the contact regions enhances the tortuosity of the fracture, the overall reduction of the space size of the whole fracture weaken the existence of sharp geometries, thus reduces the range of the eddy flow behind the contact spots (Fig. 16-d). More comprehensive discussion regarding these is given in Section 5.3.

The micro-changes of the eddy flow determine the occurrence of the macro non-Darcy characteristics. To quantitatively characterize the onset of the transition from linear flow to non-Darcy flow, the critical Reynolds number  $Re_c$  is determined. Here, taking the widely-used critical  $E = 0.1$  as the critical condition (Zimmerman et al. 2004; Zhang and Némcik 2013; Chen et al. 2015), the calculation results of the critical Reynolds numbers  $Re_c$  can be obtained through combining the Eqs. (8) and (9). The parameters A and B in Eq. (9) are obtained from fitting the relation between pressure gradient and flow rates with the Forchheimer's equation Eq. (4). Fig. 18 shows the variations of the critical Reynolds number  $Re_c$  for the rough fracture with the hydraulic apertures, which demonstrates that both them decrease nonlinearly as the hydraulic apertures increases between the 0.035 mm to 0.165 mm. The possible reason for this change is seen in Fig. 17 in the above discussion.

The significant decrease of the aperture and sharp geometries in the rock fracture under the high confine stress reduces the range of the eddy flow, which delays the occurrence of the significant inertial effects, finally leading to the increase of critical Reynolds numbers with the hydraulic aperture decreases. Similar results are also observed in the work by Zhou et al. (2015), in which the critical Reynolds number  $Re_c$  also presents a downward tendency as the hydraulic aperture increases. However, the  $Re_c$  present decreases with the hydraulic aperture decreasing from 0.03 mm to 0.035 mm, which mainly ascribed to the increasing tortuosity of the flow channel, caused by the more and more contacts under the high confine stress, where the fracture aperture varied slightly and the non-Darcy behavior in the rough fracture are determined by the contacts. The similar results are also discussed in the work by Chen et al. (2019)

### 5.2. Mechanism analysis on non-Darcy flow caused by fracture geometries

As discussed above, the asperity contact is a critical geometric structure that complicates the water pressure variations and causes the

non-Darcy flow in rough fracture. To more clearly demonstrate the mechanism by this influences the water pressure distribution and non-Darcy in the 3D real fracture models, a simplified 3D representative micro-model, with an idealized cubic geometric feature including both the asperity contact (non-zero small aperture  $1\ \mu\text{m}$ ) and the void spaces, was built (Fig. 19). The micro model provides a better representation of micro-geometries that are common in any rough rock fracture (Fig. 19-b). In the following, six different models with the same contact region of  $1\ \mu\text{m}$  and different fracture apertures of 0.01 mm, 0.02 mm, 0.03 mm, 0.04 mm, 0.08 mm and 0.1 mm were implemented to observe the water pressure variations and the possible eddy flows occurs in the micro models. The initial and boundary conditions mentioned in the manuscript were applied and the constant injection flow rates of  $2\text{E-}8\ \text{m}^3/\text{s}$  ( $Re = 20$ ), was kept along the inlet end.

Fig. 20 shows the decrease in normalized water pressure along the monitoring line  $Y = 0.44\ \text{mm}$  located closed to the bottom of the model. The light blue color marks the location of the contact. The contact regions make it difficult for the fluid to flow through; this results in a non-linear decrease in the water pressure. The deviation of them from the linear was indicated in Fig. 20, which becomes more noticeable as the fracture aperture increases. Under the same injection rate, when the fracture aperture is low, the streamlines are continuous and no significant closed curve eddies formed (Fig. 21-b and c). As the aperture increase, swirling backflows or eddies easily occur behind the contact regions and will continue to form helical variation around these areas as the aperture increases (Fig. 21-d, e, f, g). These features of eddy flow are similar to those observations in simulations in Fig. 17, revealing that the contact regions formed in a rock fracture result in more complicated flow features and lead to complex changes in the water pressure.

### 5.3. Limitations

The present study focuses on the fluid flow in 3D real rough fractures with geometry changes under confine stresses, and thus we consider the one-way coupling of stress effect on apertures, but the hydro-mechanical behavior, resulted from high water pressure, are worth of systematic studies in future. The increase in the water pressure and the resultant aperture or contact open requires the modelling of the contact processes that will be present at asperity contacts. These can either be stationary, advancing or receding, with friction and dilatancy contributing to the evolution of apertures. The topic of contact mechanics at geological interfaces needs to be incorporated to correctly address the H-M couplings (Selvadurai and Boulon 1995); These aspects involve the complicated coupled hydro-mechanical process in the rough fractured rock mass and will be studied in future research. Besides, the irregular distribution of the water pressure due to irregular fracture geometry also emphasizes the need for improvements to the traditional effective stress law in the rough fracture.

The aperture field under different confine stresses was obtained by removing the overlaps between the two surfaces, and the elastic and plastic deformation between different micro asperities, are not considered. Solving the elastic or plastic deformation problem would be more rigorous and does lead to different fracture geometry, especially at high confine stress. The special treatment that assigns very small aperture values to the contact elements was also improved to obtain more precise results. These aspects will be studied in future research. Besides, the asperity degradation occurred under high confine stress affects the aperture distribution and also eddy flow, further affecting the heterogeneous pressure distribution and fluid overpressure related to the onset of fracture instability (Ji and Wu 2020). Theoretical research and micro measurement are needed to reveal this complicated process in future research. In addition, the flow simulation within the entire rock sample instead of the small size of the sample needs to be further conducted for more accurate simulation results

## 6. Conclusions

A series of fracture geometries of an artificially tensile fractured sandstone sample, measured during the hydraulic tests at increasing confine stresses, by using the point cloud matching method, was adopted to build 3D real fracture models; At each stress stage, a variety of flow simulations with increasing fluid injection rates from  $3.33\text{E-}8\ \text{m}^3/\text{s}$  to  $3.33\text{E-}5\ \text{m}^3/\text{s}$ , corresponding to Reynolds numbers  $Re$  from 2.22 to 2220, were obtained by solving the Navier-Stokes equations. The simulated apparent transmissivity in the 3D real fractures under increasing confine stress are compared with that measured from hydraulic flow tests. The impact of voids and contact alterations due to stress loading was studied to assess how they affected the flow characteristics within the 3D real rough fractures. The non-Darcy flow characteristic and the related causing mechanism under the increasing confine stress were discussed. The main conclusions include:

- 1) Both the measured and simulated transmissivity decreases exponentially with the increase in confine stresses, and the simulation values match well with that measured at each stress level, under the inflow rates of  $3.33\text{E-}8\ \text{m}^3/\text{s}$  and  $3.33\text{E-}7\ \text{m}^3/\text{s}$ , respectively. The flow capacity in real 3D fractures subjected to the confine stress can be described well using full N-S equations. This provides a reasonable basis for the flow characteristics representation within the rock fractures under the high confine stress, including the distribution of velocities, streamlines, inner water pressure, as well as the non-Darcy flow, which cannot be easily observed in tests.
- 2) The alterations in asperity contacts and void spaces due to stress changes increase the heterogeneities of the flow characteristics in 3D rough rock fracture, including flow velocities, streamlines, water pressure and non-Darcy flow behaviors. The streamlines form within the larger apertures and become more channeled with observable tortuosity under increasing confine stress. The locations of contact are the main cause of the deviations in the linear streamlines. The distribution of contact regions within fractures brings high water resistance and results in the reduced decay of the water pressure. The increase of contact regions due to confine stress enhances the non-linearity of the pressure drop in real fractures.
- 3) The eddy flows caused by high inflow rates cause the local fluctuation of water pressure and lead to more deviation of water pressure from the linearity, but not change the global non-linear decrease tendency in the 3D rock fractures. The significant decrease of both the aperture and sharp geometries in the rock fracture under the high confine stress reduces the range of the eddy flow, which delays the occurrence of the significant inertial effects, finally leading to the increase of critical Reynolds numbers with the hydraulic aperture decreases. These features can be interpreted well through analyzing the flow characteristics in an idealized 3D representative micro geometric including both the asperity contact and the void spaces.

### CRedit authorship contribution statement

**Yuedu Chen:** Conceptualization, Methodology, Software, Data curation, Writing - original draft. **A.P.S. Selvadurai:** Formal analysis, Writing - review & editing. **Zhihong Zhao:** Writing - review & editing.

### Declaration of Competing Interest

The authors declare that they have no known competing financial interests or personal relationships that could have appeared to influence the work reported in this paper.

### Acknowledgements

This work was supported by the Postdoctoral Research Foundation of China (2019TQ0174, 2019M660652) and the National Natural Science

Foundation of China (Nos. 51779123). The first author acknowledges support from the China Scholarship Council (No.201706930018). The work was prepared during the China Scholarship Council visit to the Environmental Geomechanics Laboratory at the Department of Civil Engineering and Applied Mechanics, McGill University, Montréal, Canada.

## References

- Bear, J., 1972. *Dynamics of fluids in porous media*. Elsevier, News York.
- Brown, S.R., 1989. Transport of fluid and electric current through a single fracture. *J Geophys Res Solid Earth* 94, 9429–9438. <https://doi.org/10.1029/JB094iB07p09429>.
- Cappa F, Scuderi MM, Collettini C, et al (2019) Stabilization of fault slip by fluid injection in the laboratory and in situ. *Sci Adv* 5:eau4065. <http://doi.org/10.1126/sciadv.aau4065>.
- Cardenas, M.B., Slottke, D.T., Ketcham, R.A., Sharp Jr, J.M., 2007. Navier-Stokes flow and transport simulations using real fractures shows heavy tailing due to eddies. *Geophys Res Lett* 34, L14404. <https://doi.org/10.1029/2007GL030545>, 2007.
- Chen, Y., Lian, H., Liang, W., et al., 2019. The influence of fracture geometry variation on non-Darcy flow in fractures under confining stresses. *Int J Rock Mech Min Sci* 113, 59–71.
- Chen, Y., Liang, W., Lian, H., et al., 2017. Experimental study on the effect of fracture geometric characteristics on the permeability in deformable rough-walled fractures. *Int J Rock Mech Min Sci* 98, 121–140.
- Chen, Y., Selvadurai, A.P.S., Liang, W., 2018. Computational Modelling of Groundwater Inflow During a Longwall Coal Mining Advance: A Case Study from the Shanxi Province, China. *Rock Mech Rock Eng* 52, 917–934. <https://doi.org/10.1007/s00603-018-1603-1>.
- Chen, Y., Zhao, Z., 2020. Heat transfer in a 3D rough rock fracture with heterogeneous apertures. *Int J Rock Mech Min Sci* 134, 104445. <https://doi.org/10.1016/j.ijrmmms.2020.104445>.
- Chen, Y.F., Zhou, J.Q., Hu, S.H., et al., 2015. Evaluation of Forchheimer equation coefficients for non-Darcy flow in deformable rough-walled fractures. *J Hydrol* 529, 993–1006. <https://doi.org/10.1016/j.jhydrol.2015.09.021>.
- Choi, H., Jeon, W.-P., Kim, J., 2008. Control of flow over a bluff body. *Annu Rev Fluid Mech* 40, 113–139.
- Crandall, D., Bromhal, G., Karpyn, Z.T., 2010. Numerical simulations examining the relationship between wall-roughness and fluid flow in rock fractures. *Int J Rock Mech Min Sci* 47, 784–796. <https://doi.org/10.1016/j.ijrmmms.2010.03.015>.
- Detwiler, R.L., Rajaram, H., Glass, R.J., 2000. Solute transport in variable-aperture fractures: An investigation of the relative importance of Taylor dispersion and macrodispersion. *Water Resour Res* 36, 1611–1625. <https://doi.org/10.1029/2000WR900036>.
- Develi, K., Babadagli, T., 2015. Experimental and visual analysis of single-phase flow through rough fracture replicas. *Int J Rock Mech Min Sci* 73, 139–155. <https://doi.org/10.1016/j.ijrmmms.2014.11.002>.
- Forchheimer, P., 1901. *Wasserbewegung durch Boden*. *ZVDI* 45, 1782–1788.
- Gangi, A.F., 1978. Variation of whole and fractured porous rock permeability with confining pressure. *Int J Rock Mech Min Sci Geomech Abstr* 15, 249–257. [https://doi.org/10.1016/0148-9062\(78\)90957-9](https://doi.org/10.1016/0148-9062(78)90957-9).
- Huang, N., Liu, R., Jiang, Y., 2017. Numerical study of the geometrical and hydraulic characteristics of 3D self-affine rough fractures during shear. *J Nat Gas Sci Eng* 45, 127–142. <https://doi.org/10.1016/j.jngse.2017.05.018>.
- Indraratna, B., Kumara, C., Zhu, S.-P., Sloan, S., 2015. Mathematical modeling and experimental verification of fluid flow through deformable rough rock joints. *Int J Geomech* 15, 4014065. [https://doi.org/10.1061/\(ASCE\)GM.1943-5622.0000413](https://doi.org/10.1061/(ASCE)GM.1943-5622.0000413).
- Ishibashi, T., Watanabe, N., Hirano, N., et al., 2015. Beyond-laboratory-scale prediction for channeling flows through subsurface rock fractures with heterogeneous aperture distributions revealed by laboratory evaluation. *J Geophys Res Solid Earth* 120, 106–124. <https://doi.org/10.1002/2014JB011555>.
- Javadi, M., Sharifzadeh, M., Shahriar, K., 2010. A new geometrical model for non-linear fluid flow through rough fractures. *J Hydrol* 389, 18–30. <https://doi.org/10.1016/j.jhydrol.2010.05.010>.
- Javadi, M., Sharifzadeh, M., Shahriar, K., Mitani, Y., 2014. Critical Reynolds number for nonlinear flow through rough-walled fractures: The role of shear processes. *Water Resour Res* 50, 1789–1804. <https://doi.org/10.1002/2013WR014610>.
- Ji, Y., Wanniarachchi, W.A.M., Wu, W., 2020. Effect of fluid pressure heterogeneity on injection-induced fracture activation. *Comput Geotech* 123, 103589. <https://doi.org/10.1016/j.compgeo.2020.103589>.
- Ji, Y., Wu, W., 2020. Injection-driven fracture instability in granite: Mechanism and implications. *Tectonophysics* 791, 228572. <https://doi.org/10.1016/j.tecto.2020.228572>.
- Jia, Y., Wu, W., Kong, X.Z., 2020. Injection-induced slip heterogeneity on faults in shale reservoirs. *Int J Rock Mech Min Sci* 131, 104363. <https://doi.org/10.1016/j.ijrmmms.2020.104363>.
- Jing, L., 2003. A review of techniques, advances and outstanding issues in numerical modelling for rock mechanics and rock engineering. *Int J Rock Mech Min Sci* 40, 283–353. [https://doi.org/10.1016/S1365-1609\(03\)00013-3](https://doi.org/10.1016/S1365-1609(03)00013-3).
- Kong, B., Chen, S., 2018. Numerical simulation of fluid flow and sensitivity analysis in rough-wall fractures. *J Pet Sci Eng* 168, 546–561. <https://doi.org/10.1016/j.petrol.2018.04.070>.
- Koyama, T., Li, B., Jiang, Y., Jing, L., 2009. Numerical modelling of fluid flow tests in a rock fracture with a special algorithm for contact areas. *Comput Geotech* 36, 291–303. <https://doi.org/10.1016/j.compgeo.2008.02.010>.
- Koyama, T., Neretnieks, I., Jing, L., 2008. A numerical study on differences in using Navier-Stokes and Reynolds equations for modeling the fluid flow and particle transport in single rock fractures with shear. *Int J Rock Mech Min Sci* 45, 1082–1101. <https://doi.org/10.1016/j.ijrmmms.2007.11.006>.
- Kundu, P.K., Cohen, I.M., 2008. *Fluid Mechanics*, 4th edn. Elsevier Academic Press, San Diego.
- Lee, S.H., Lee, K.K., Yeo, I.W., 2014. Assessment of the validity of Stokes and Reynolds equations for fluid flow through a rough-walled fracture with flow imaging. *Geophys Res Lett* 41, 4578–4585. <https://doi.org/10.1002/2014GL060481>.
- Lee, S.H., Yeo, I.W., Lee, K.K., Detwiler, R.L., 2015. Tail shortening with developing eddies in a rough-walled rock fracture. *Geophys Res Lett* 42, 6340–6347. <https://doi.org/10.1002/2015GL065116>.
- Li, B., Jiang, Y., Koyama, T., et al., 2008. Experimental study of the hydro-mechanical behavior of rock joints using a parallel-plate model containing contact areas and artificial fractures. *Int J Rock Mech Min Sci* 45, 362–375. <https://doi.org/10.1016/j.ijrmmms.2007.06.004>.
- Li, B., Liu, R., Jiang, Y., 2016. Influences of hydraulic gradient, surface roughness, intersecting angle, and scale effect on nonlinear flow behavior at single fracture intersections. *J Hydrol* 538, 440–453. <https://doi.org/10.1016/j.jhydrol.2016.04.053>.
- Liu, R., Huang, N., Jiang, Y., et al., 2020. A numerical study of shear-induced evolutions of geometric and hydraulic properties of self-affine rough rock fractures. *Int J Rock Mech Min Sci* 127, 104211. <https://doi.org/10.1016/j.ijrmmms.2020.104211>.
- Mofakham, A.A., Stadelman, M., Ahmadi, G., et al., 2018. Computational Modeling of Hydraulic Properties of a Sheared Single Rock Fracture. *Transp Porous Media* 124, 1–30. <https://doi.org/10.1007/s11242-018-1030-5>.
- Nazridoust, K., Ahmadi, G., Smith, D.H., 2006. A new friction factor correlation for laminar, single-phase flows through rock fractures. *J Hydrol* 329, 315–328. <https://doi.org/10.1016/j.jhydrol.2006.02.032>.
- Niya, S.M.R., Selvadurai, A.P.S., 2019. Correlation of joint roughness coefficient and permeability of a fracture. *Int J Rock Mech Min Sci* 113, 150–162. <https://doi.org/10.1016/j.ijrmmms.2018.12.008>.
- Pyrak-Nolte, L.J., Nolte, D.D., 2016. Approaching a universal scaling relationship between fracture stiffness and fluid flow. *Nat Commun* 7, 10663. <https://doi.org/10.1038/ncomms10663>.
- Raven, K.G., Gale, J.E., 1985. Water flow in a natural rock fracture as a function of stress and sample size. *Int J Rock Mech Min Sci* 22, 251–261. [https://doi.org/10.1016/0148-9062\(85\)92952-3](https://doi.org/10.1016/0148-9062(85)92952-3).
- Renshaw, C.E.E., 1995. On the relationship between mechanical and hydraulic apertures in rough-walled fractures. *J Geophys Res Solid Earth* 100, 24629–24636. <https://doi.org/10.1029/95JB02159>.
- Rong, G., Yang, J., Cheng, L., Zhou, C., 2016. Laboratory investigation of nonlinear flow characteristics in rough fractures during shear process. *J Hydrol* 541, 1385–1394.
- Rutqvist, J., Stephansson, O., 2003. The role of hydrochemical coupling in fractured rock engineering. *Hydrogeol J* 11, 7–40.
- Schrauf, T.W., Evans, D.D., 1986. Laboratory Studies of Gas Flow Through a Single Natural Fracture. *Water Resour Res* 22, 1038–1050. <https://doi.org/10.1029/WR022i007p01038>.
- Selvadurai, A.P.S., 2015. Normal stress-induced permeability hysteresis of a fracture in a granite cylinder. *Geofluids* 15, 37–47. <https://doi.org/10.1111/gf.12107>.
- Selvadurai, A.P.S., Boulon, M.J., 1995. *Mechanics of geomaterial interfaces*. *Studies in Applied Mechanics*, Vol. 42. Elsevier, Amsterdam, The Netherlands.
- Selvadurai, A.P.S., Couture, C.B., Rezaei Niya, S.M., 2017. Permeability of wormholes created by CO<sub>2</sub>-acidized water flow through stressed carbonate rocks. *Phys Fluids* 29, 096604. <https://doi.org/10.1063/1.5002129>.
- Selvadurai, A.P.S., Suvorov, A.P., Selvadurai, P.A., 2015. Thermo-hydro-mechanical processes in fractured rock formations during a glacial advance. *Geosci Model Dev* 8, 2167–2185. <https://doi.org/10.5194/gmd-8-2167-2015>.
- Selvadurai, A.P.S., Zhang, D., Kang, Y., 2018. Permeability evolution in natural fractures and their potential influence on loss of productivity in ultra-deep gas reservoirs of the Tarim Basin, China. *J Nat Gas Sci Eng* 58, 162–177. <https://doi.org/10.1016/j.jngse.2018.07.026>.
- Singh, K.K., Singh, D.N., Ranjith, P.G., 2015. Laboratory simulation of flow through single fractured granite. *Rock Mech Rock Eng* 48, 987–1000. <https://doi.org/10.1007/s00603-014-0630-9>.
- Stoll, M., Huber, F.M., Trumm, M., et al., 2019. Experimental and numerical investigations on the effect of fracture geometry and fracture aperture distribution on flow and solute transport in natural fractures. *J Contam Hydrol* 221, 82–97. <https://doi.org/10.1016/j.jconhyd.2018.11.008>.
- Tsang, Y.W., Witherspoon, P.A., 1981. Hydromechanical behavior of a formable rock fracture subject to normal stress. *J Geophys Res* 86, 9287–9298. <https://doi.org/10.1029/JB086iB10p09287>.
- Wang, L., Cardenas, M.B., Slottke, D.T., et al., 2015. Modification of the Local Cubic Law of fracture flow for weak inertia, tortuosity, and roughness. *Water Resour Res* 51, 2064–2080. <https://doi.org/10.1002/2014WR015815>.
- Wang, M., Chen, Y.F., Ma, G.W., et al., 2016. Influence of surface roughness on nonlinear flow behaviors in 3D self-affine rough fractures: Lattice Boltzmann simulations. *Adv Water Resour* 96, 373–388. <https://doi.org/10.1016/j.advwatres.2016.08.006>.
- Xie, L.Z., Gao, C., Ren, L., Li, C.B., 2015. Numerical investigation of geometrical and hydraulic properties in a single rock fracture during shear displacement with the Navier-Stokes equations. *Environ Earth Sci* 73, 7061–7074. <https://doi.org/10.1007/s12665-015-4256-3>.

- Xiong, F., Jiang, Q., Chen, M., 2018. Numerical Investigation on Hydraulic Properties of Artificial-Splitting Granite Fractures during Normal and Shear Deformations. *Geofluids*. <https://doi.org/10.1155/2018/9036028>.
- Xiong, X., Li, B., Jiang, Y., et al., 2011. Experimental and numerical study of the geometrical and hydraulic characteristics of a single rock fracture during shear. *Int J Rock Mech Min Sci* 48, 1292–1302. <https://doi.org/10.1016/j.ijrmms.2011.09.009>.
- Yeo, I.W., De Freitas, M.H., Zimmerman, R.W., 1998. Effect of shear displacement on the aperture and permeability of a rock fracture. *Int J Rock Mech Min Sci* 35, 1051–1070. [https://doi.org/10.1016/S0148-9062\(98\)00165-X](https://doi.org/10.1016/S0148-9062(98)00165-X).
- Zhang, Q., Ju, Y., Gong, W., et al., 2015. Numerical simulations of seepage flow in rough single rock fractures. *Petroleum* 1, 200–205. <https://doi.org/10.1016/j.petim.2015.09.003>.
- Zhang, Z., Nemeik, J., 2013. Fluid flow regimes and nonlinear flow characteristics in deformable rock fractures. *J Hydrol* 477, 139–151. <https://doi.org/10.1016/j.jhydrol.2012.11.024>.
- Zhang, Z., Nemeik, J., Ma, S., 2013. Micro-and macro-behaviour of fluid flow through rock fractures: an experimental study. *Hydrogeol J* 21, 1717–1729. <https://doi.org/10.1007/s10040-013-1033-9>.
- Zhao, J., Brown, E.T., 1992. Hydro-thermo-mechanical properties of joints in the Carnmenellis granite. *Q J Eng Geol Hydrogeol* 25, 279–290. <https://doi.org/10.1144/GSL.QJEG.1992.025.04.03>.
- Zhao, Z., 2014. On the heat transfer coefficient between rock fracture walls and flowing fluid. *Comput Geotech* 59, 105–111. <https://doi.org/10.1016/j.compgeo.2014.03.002>.
- Zhao, Z., Jing, L., Neretnieks, I., Moreno, L., 2011. Numerical modeling of stress effects on solute transport in fractured rocks. *Comput Geotech* 38, 113–126. <https://doi.org/10.1016/j.compgeo.2010.10.001>.
- Zhou, J.Q., Hu, S.H., Fang, S., et al., 2015. Nonlinear flow behavior at low Reynolds numbers through rough-walled fractures subjected to normal compressive loading. *Int J Rock Mech Min Sci* 80, 202–218.
- Zimmerman, R., Bodvarsson, G., 1996. Hydraulic conductivity of rock fractures. *Transp Porous Media* 23, 1–30. <https://doi.org/10.1007/BF00145263>.
- Zimmerman, R.W., Al-Yaarubi, A., Pain, C.C., Grattoni, C.A., 2004. Non-linear regimes of fluid flow in rock fractures. *Int J Rock Mech Min Sci* 41, 163–169. <https://doi.org/10.1016/j.ijrmms.2004.03.036>.
- Zimmerman, R.W., Chen, D.W., Cook, N.G.W., 1992. The effect of contact area on the permeability of fractures. *J Hydrol* 139, 79–96.
- Zou, L., Jing, L., Cvetkovic, V., 2015. Roughness decomposition and nonlinear fluid flow in a single rock fracture. *Int J Rock Mech Min Sci* 75, 102–118. <https://doi.org/10.1016/j.ijrmms.2015.01.016>.
- Zou, L., Jing, L., Cvetkovic, V., 2017a. Shear-enhanced nonlinear flow in rough-walled rock fractures. *Int J Rock Mech Min Sci* 97, 33–45. <https://doi.org/10.1016/j.ijrmms.2017.06.001>.
- Zou, L., Jing, L., Cvetkovic, V., 2017b. Modeling of flow and mixing in 3D rough-walled rock fracture intersections. *Adv Water Resour.* <https://doi.org/10.1016/j.advwatres.2017.06.003>.